

Official Journal of Turkish Society of Magnetic Resonance

CRMRI

Current Research in MRI

**Intrahepatic Biliary Variations on Magnetic Resonance
Cholangiopancreatography: A Study From a Tertiary Centre
in North East India**

Donboklang Lynser, Chhunthang Daniala, Panchasanguparakalarajan R,
Praveen Kumar Chinniah

**Evaluation of Magnetic Resonance Imaging Findings of
COVID-19-Related Rhino-Orbito-Cerebral Mucormycosis**

Bişar Akbaş, Bedir Kaya, Ahsen Çavuşoğlu Akbaş, Nazlı Nida Kaya,
Ömer Kaya, Figen Binokay, Yunus Kenan Bıçakçı

**The Relationship Between Patellar Chondromalacia
and Patellofemoral Joint Anatomical Variations**

Can Usal, Atilla Hikmet Çilengir, Orkun Sarıoğlu,
Berna Dirim Mete, Özgür Tosun

**Magnetic Resonance Imaging Assessment of
Normal ADC Values of the Parotid Gland**

Ömer Kazcı, Bünyamin Ece

Editor in Chief

Mecit Kantarcı 

Department of Radiology, Erzincan Binali Yıldırım University, Faculty of Medicine; Atatürk University, Faculty of Medicine, Erzincan, Erzurum, Turkey

Editors

Abdominal Radiology

Aytekin Oto 

The University of Chicago, Department of Radiology, Chief Physician, Head of the Faculty Practice Plan and Dean for Clinical Affairs, Chicago, USA

Murat Danacı 

Department of Radiology, Ondokuz Mayıs University, Faculty of Medicine, Samsun, Turkey

Breast Radiology

Serap Gültekin 

Department of Radiology, Gazi University, Faculty of Medicine, Ankara, Turkey

Cardiac Radiology

Memduh Dursun 

Department of Radiology, İstanbul University, İstanbul Faculty of Medicine, İstanbul, Turkey

Cihan Duran 

Department of Diagnostic and Interventional Imaging, The University of Texas, McGovern Medical School, Texas, USA

Emergency Radiology

Mehmet Ruhi Onur 

Department of Radiology, Hacettepe University Faculty of Medicine Hospital, Ankara, Turkey

Engineer Group

Esin Öztürk Işık 

Biomedical Engineering, Boğaziçi University, İstanbul, Turkey

Head & Neck Radiology

Nafi Aygün 

Department of Radiology, Johns Hopkins University School of Medicine, Baltimore, Maryland, USA

Hatice Gül Hatipoğlu 

Department of Radiology, Health Science University, Gulhane Faculty of Medicine, Ankara Bilkent City Hospital, Ankara, Turkey

Musculoskeletal Radiology

Nil Tokgöz 

Department of Radiology, Gazi University, Faculty of Medicine, Ankara, Turkey

Neuroradiology Radiology


Alpay Alkan 

Department of Radiology, Bezmialem Vakıf University, Faculty of Medicine, İstanbul, Turkey

Pediatric Radiology

Korgün Koral 

Department of Radiology, University of Texas Southwestern Medical Center, Dallas, TX, USA

Süreyya Burcu Görkem 

Department of Pediatric Radiology, Adana State Hospital, Adana, Turkey

Thorax Radiology

Polat Koşucu 

Department of Radiology, Karadeniz Teknik University, Faculty of Medicine, Trabzon, Turkey

Biostatistical Consultant

Sonay Aydın 

Department of Radiology, Erzincan Binali Yıldırım University, Faculty of Medicine, Erzincan, Turkey



Founder

İbrahim KARA

General Manager

Ali ŞAHİN

Finance Coordinator

Elif YILDIZ ÇELİK

Journal Managers

İrem SOYSAL

Bahar ALBAYRAK

Deniz KAYA

İrmak BERBEROĞLU

Publications Coordinators

Gökhan ÇİMEN

Arzu ARI

Alara ERGİN

Hira Gizem FİDAN

İrem ÖZMEN

Project Coordinators

Doğan ORUÇ

Sinem Fehime KOZ

Contact

Address: Büyükdere Cad. No: 105/9

34394 Mecidiyeköy, Şişli-İstanbul

Phone: +90 212 217 17 00

E-mail: info@avesyayincilik.com

AIMS AND SCOPE

Current Research in MRI (Curr Res MRI) is a scientific, open access, online-only official publication of the Turkish Society of Magnetic Resonance published in accordance with independent, unbiased, and double-blinded peer-review principles. The journal is published triannually in April, August, and December. The publication language of the journal is English.

Current Research in MRI aims to contribute to the literature by publishing manuscripts at the highest scientific level on radiology. The journal publishes original articles, reviews, case reports, and letters to the editor that are prepared in accordance with ethical guidelines.

The target audience of the journal includes specialists, researchers and professionals who working and interested in the field of radiology.

The editorial and publication processes of the journal are shaped in accordance with the guidelines of the International Committee of Medical Journal Editors (ICMJE), World Association of Medical Editors (WAME), Council of Science Editors (CSE), Committee on Publication Ethics (COPE), European Association of Science Editors (EASE), and National Information Standards Organization (NISO). The journal is in conformity with the Principles of Transparency and Best Practice in Scholarly Publishing (doaj.org/bestpractice).

Publication Fee Policy

All expenses of the journal are covered by the Turkish Society of Magnetic Resonance. Processing and publication are free of charge with the journal. No fees are requested from the authors at any point throughout the evaluation and publication process. All manuscripts must be submitted via the online submission system, which is available at <http://curremr.com>. The journal guidelines, technical information, and the required forms are available on the journal's web page.

Advertisement Policy

Current Research in MRI can publish advertisement images in the journal's website upon the approval of the Editor in

Chief. Potential advertisers should contact the Editorial Office. Advertisers have no effect on the editorial decisions or advertising policies.

Disclaimer

Statements or opinions expressed in the manuscripts published in the journal reflect the views of the author(s) and not the opinions of the editors, editorial board, and/or publisher; the editors, editorial board, and publisher disclaim any responsibility or liability for such materials.

Open Access Statement

Current Research in MRI is an open access publication, and the journal's publication model is based on Budapest Access Initiative (BOAI) declaration. All published content is available online, free of charge at <http://curremr.com>. The journal's content is licensed under a Creative Commons Attribution-NonCommercial (CC BY-NC) 4.0 International License which permits third parties to share and adapt the content for non-commercial purposes by giving the appropriate credit to the original work.

You can reach the current version of the instructions to authors at <https://curremr.com/EN>

Editor in Chief: Mecit Kantarcı

Address: Department of Radiology, Erzincan Binali Yıldırım University School of Medicine, Erzincan, Turkey

E-mail: akkanrad@hotmail.com

Publisher: Turkish Society of Magnetic Resonance

Address: Konak Mah. 858. Sok. No: 2 Çakıroğlu İş Hanı Kat: 5 Daire: 55 Konak / İzmir, Turkey

Publishing Service: AVES

Address: Büyükdere Cad., 105/9 34394 Şişli, İstanbul, Turkey

Phone: +90 212 217 17 00

E-mail: info@avesyayincilik.com

Webpage: www.avesyayincilik.com

CONTENTS

ORIGINAL ARTICLES

- 1 Intrahepatic Biliary Variations on Magnetic Resonance Cholangiopancreatography: A Study From a Tertiary Centre in North East India
Donboklang Lynser, Chhunthang Daniala, Panchasanguparakalarajan R, Praveen Kumar Chinniah
- 6 Evaluation of Magnetic Resonance Imaging Findings of COVID-19-Related Rhino-Orbito-Cerebral Mucormycosis
Bişar Akbaş, Bedir Kaya, Ahsen Çavuşoğlu Akbaş, Nazlı Nida Kaya, Ömer Kaya, Figen Binokay, Yunus Kenan Bıçakçı
- 11 The Relationship Between Patellar Chondromalacia and Patellofemoral Joint Anatomical Variations
Can Usal, Atilla Hikmet Çilengir, Orkun Sarioğlu, Berna Dirim Mete, Özgür Tosun
- 16 Magnetic Resonance Imaging Assessment of Normal ADC Values of the Parotid Gland
Ömer Kazıcı, Bünyamin Ece

CASE REPORT

- 19 Case Report and Review of Literature of Van-Neck Odelberg Disease: A Challenging Differential Diagnosis for Pelvic Fractures
Nur Hürsoy, Lütfullah Sağır, Elif Arzu Özen, Fatma Beyazal Çeliker

Intrahepatic Biliary Variations on Magnetic Resonance Cholangiopancreatography: A Study From a Tertiary Centre in North East India

Donboklang Lynser¹, Chhunthang Daniala¹, Panchasanguparakalarajan R¹, Praveen Kumar Chinniah²

¹Department of Radiology and Imaging, North Eastern Indira Gandhi Regional Institute of Health and Medical Sciences, Mawdiangdiang, Meghalaya, India

²Department of Radiology, Christian Medical College Tamil Nadu, India

Cite this article as: Lynser D, Daniala C, Panchasanguparakalarajan R, Chinniah, PK. Intrahepatic biliary variations on magnetic resonance cholangiopancreatography: A study from a tertiary centre in North East India. *Current Research in MRI*, 2023;2(1):1-5.

Corresponding author: Donboklang Lynser, e-mail: bokdlynser@gmail.com

Received: February 2, 2023 **Accepted:** March 30, 2023 **Publication Date:** April 24, 2023

DOI:10.5152/CurrResMRI.2023.23051



Content of this journal is licensed under a Creative Commons Attribution-NonCommercial 4.0 International License.

Abstract

Objective: It is known that variations can occur in the insertion of biliary ducts in both right and left intrahepatic ductal systems. We undertake this study to evaluate the normal anatomy and variations of intrahepatic biliary system on magnetic resonance cholangiopancreatography, classify them into typical and atypical right hepatic duct and left hepatic duct, and compare relationships between them.

Methods: This is a 10-year retrospective study (2008-2018). Magnetic resonance cholangiopancreatography using a 1.5 T Siemens with breath-hold HASTE sequence, FS HASTE, thin slice FSE T2-WI with post processing volume rendered of maximum intensity projection (MIP) images. Drainage patterns were reviewed.

Results: A total of 347 cases in 10 years were analyzed (2008-2018), with age ranges from 1 year 11 months to 90 years, with a mean of 42.37 years and M : F: 145 : 202=0.71. Right posterior sectoral duct joining right anterior sectoral duct medially to form right hepatic duct was seen in 250 cases (72%), trifurcation in 59 (17%), right posterior sectoral duct joining the left hepatic duct in 20 (5.7%), right posterior sectoral duct to common hepatic duct in 10 (2.9%), aberrant right hepatic duct to cystic duct in 1 (0.3%), accessory right hepatic duct in 2 (0.58%), segment II/III draining independently into common hepatic duct/ common bile duct (CBD) in 3 (0.86%), and unclassified in 2 (0.58%) cases. The common trunk of segment II and segment III joining segment IV forming left hepatic duct was seen in 325 cases (93.7%). Comparing right hepatic duct and left hepatic duct, the tabulated Chi-square value (critical value) was 51.18 (0.001) and calculated value was 1.958 (<value at 1% level of significance) at $df=24$, The data collected were highly significant. Therefore, typical right hepatic duct drainage will also be likely to have typical left hepatic duct drainage.

Conclusion: Right posterior sectoral duct joining right anterior sectoral duct medially forming right hepatic duct and common branch of segment II and III joining the segment IV forming left hepatic duct are most common. A typical right hepatic duct insertion will most likely also be accompanied by typical drainage on the left side.

Keywords: Common hepatic duct, left hepatic duct, right anterior sectoral duct, right posterior sectoral duct, right hepatic duct, variations

INTRODUCTION

Biliary anatomy is complex, with variants seen in both intrahepatic and extrahepatic biliary ducts. Knowledge of anatomy is a prerequisite in preoperative biliary interventions, therapeutic biliary interventions liver resections, and liver transplants. Endoscopic retrograde cholangiopancreatography (ERCP) and percutaneous cholangiography techniques can clearly picture the biliary anatomy. Magnetic resonance cholangiopancreatography (MRCP), on the other hand, is a non-invasive imaging tool compared to ERCP and invasive cholangiography¹ for visualizing the biliary system. With author's experience it was found that the variants are not routinely documented on an MRCP report, probably being content with reporting of the various hepatobiliary pathologies only. Many authors have described different patterns of biliary anatomy drainage.¹ Normally a right posterior sectoral duct (RPSD) passes posterior to the right anterior sectoral duct (RASD) to insert on its medial aspect to finally form the right hepatic duct (RHD).² The left hepatic duct (LHD), on the other hand, is most commonly formed when a common trunk of segment II and segment III joins segment IV.^{1,2} Though there are many patterns of classifying variants in anatomy, for simplicity, we classified the variants according to that compiled by Sureka et al¹ (Table 1).²⁻⁶ With this knowledge in mind, we therefore undertook this study on the variations of the left and right intrahepatic ducts and to study their inter-relationships.

Purpose

To evaluate the normal anatomy and variations of intrahepatic biliary ductal system on MRCP, classify into typical and atypical RHD and LHD, and compare relationships between these variations.

Table 1. Anatomical Variants of the Intrahepatic Biliary Ductal System¹⁻⁶

Right hepatic duct	Left hepatic duct
Type I: Typical: RPSD joining RASD medially to form RHD	Type A: Common trunk of segment II and segment III joins segment IV
Type II: Trifurcation: Simultaneous emptying of the RASD, RPSD, and LHD into the CHD	Type B: Triconfluence of segments II, III, and IV
Type III: Anomalous drainage of RPSD	Type C: Segment II duct drains into the common trunk of segment III and segment IV
(A) RPSD joining LHD (crossover anomaly)	Type D: Others and unclassified variations
(B) RPSD joining CHD	
(C) RPSD joining cystic duct	
Type IV: Aberrant drainage of RHD into the cystic duct	
Type V: Accessory right hepatic duct	
Type VI: Segments II and III duct draining individually into the RHD or CHD	
Type VII: Others and unclassified variations	

CHD, common hepatic duct; LHD, left hepatic duct; RASD, right anterior sectoral duct; RHD, right hepatic duct; RPSD, right posterior sectoral duct

METHODS

This is a retrospective study on MRCP performed at our institute in 10 years (2008-2018). The study was done with the approval of the institutional ethics committee IEC at North Eastern Indira Gandhi Regional Institute of Health and Medical Sciences (Date: July 2, Number: NEIGR/IEC/M8/F12/19). Consent was waived as this was a retrospective study. Exclusion criteria are post-operative, grossly dilated biliary system distorting anatomy, malignant condition at the confluence and common hepatic duct (CHD), degraded images, post-transplant, pneumobilia, stents, traumatic conditions, and all other conditions that severely distort the anatomy and image quality.

Magnetic resonance imaging (MRI) was performed using 1.5 T units (Siemens MAGNETOM, Avanto, Belgium Made). The MRCP protocol includes breath-hold HASTE sequence, axial and coronal FS HASTE, thin slice fast spin echo T2-WI along with post processing volume rendered of MIP images.

The images were reviewed and variations of the RHD, LHD, and confluence were classified as in Table 1. The images were reviewed by consensus of 2 experienced radiologists at a time (minimum of 3 years experience in hepatobiliary imaging) on a Syngo.via reading solution in our MRI console.

Statistical Analysis

Descriptive statistics was done using chi-square test.

RESULTS

A total of 347 cases in 10 years were analyzed (2008-2018), with age ranges from 1 year 11 months to 90 years, with a mean of 42.37 years and M:F: 145:202=0.71. For the RHD, type I-typical RHD insertion was seen in 250 cases (72%) (Figure 1). The next common insertion is the type II—trifurcation in 59 cases (17%) (Figure 2), type IIIA—RPSD joining the LHD in 20 cases (5.7%) (Figure 3), RPSD to CHD in

10 cases (2.9%), aberrant RHD to cystic duct in 1 case (0.3%), accessory RHD in 2 cases (0.58%), segments II or III draining independently into CHD or common bile duct (CBD) in 3 cases (0.86%) and unclassified in 2 cases (0.58%). Typical (type A) LHD insertion—the common trunk of segment II and segment III joining segment IV (Figure 4) was seen in 325 cases (93.7%), type B—triconfluence of segments II, III, and IV was seen in 13 cases (3.7%), type C—segment II duct draining into the common trunk of segment III and segment IV in 3 cases (0.86%) and type D—others and unclassified variations in 6 cases (1.7%).

Statistically comparing RHD and LHD, the tabulated chi-square value (critical value) was 51.18 (0.001) and the calculated value was 1.958 at *df*=24. The calculated value is much less compared to tabulated value at 1% level of significance; hence, the data collected are highly significant. Therefore, patients with type 1 (typical) RHD will

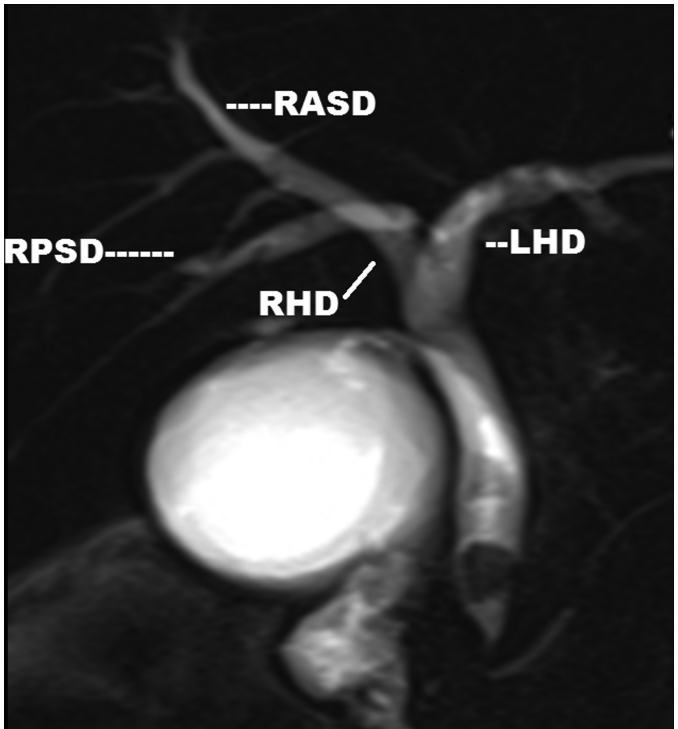


Figure 1. MRCP-T2 HASTE image showing typical insertion (type 1) of the right posterior sectoral duct (RPSD) into the medial of the right anterior sectoral duct (RASD) before becoming the right hepatic duct (RHD). MRCP, magnetic resonance cholangiopancreatography.

MAIN POINTS

- It is known that variations in the insertion of biliary ducts in both right and left intrahepatic ductal systems are common as also evident in our study.
- In our study, it is found that a typical right hepatic duct insertion is significantly associated with a typical left hepatic insertion.
- This finding can be important, especially for hepatobiliary preoperative imaging and also for the planning of biliary interventions like percutaneous transhepatic biliary drainage.

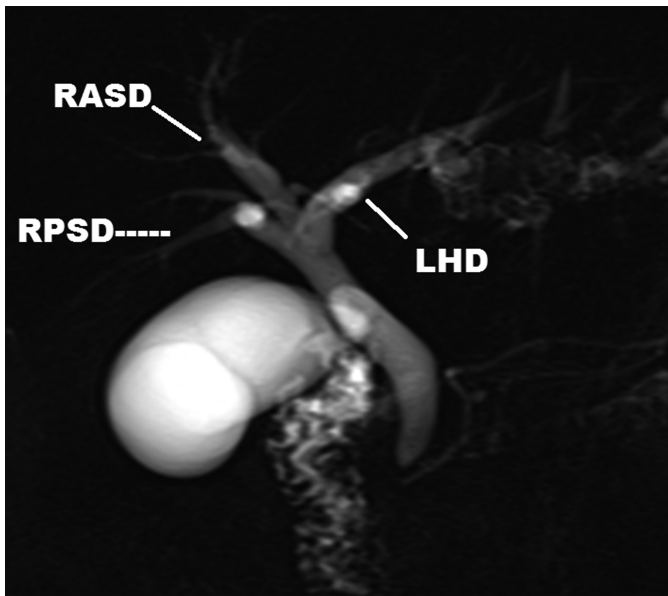


Figure 2. MRCP-T2 HASTE image showing triple confluence (type II) of the right posterior sectoral duct (RPSD), right anterior sectoral duct (RASD), and the left hepatic duct (LHD). MRCP, magnetic resonance cholangiopancreatography.

also be likely to have type A (typical) LHD, thereby accepting the null hypothesis.

DISCUSSION

This study shows the variants in the intrahepatic biliary ductal system of both the left and right lobes. In all cases, the liver was normally seen on the right side indicating normal situs. The typical RHD insertion in

our series is 72% which is comparable to other studies (Table 2). The most common atypical variant of RHD insertion is triple confluence (17%) followed by anomalous posterior sectoral duct draining to LHD (5.7%) together constituting 22.7% which together is comparable to other studies^{2,3,7} (Table 2).

Type A LHD drainage is the commonest pattern where a duct formed by the union of segments 2 (II) and 3 (III) joins the segment 4 (IV) duct to form the LHD in agreement with previous studies.^{2,5,8,9} Type A in our study is seen in 93.7% which is higher than reported in other literatures show that this pattern occurs in about 59% to 78%.^{2,5,8,9} Our series shows a higher percentage of typical LHD.

Our study also proves that a typical RHD insertion will many times mean that there will be an associated typical LHD insertion as shown in our study, but the authors suggest that this be verified individually with each case.

While so many variants in both RHD and LHD patterns have been described in the literature as discussed, knowing the anatomy of the biliary anatomy has definite clinical implications especially as a preoperative workout for my surgical and biliary interventional procedures.¹⁰ For example, variants like RPSD draining to the LHD and trifurcation can lead to inadvertent injuries on the donor during transplantation surgeries.¹¹

Unclassified anatomy can be encountered infrequently but is very rare.^{2,3,7} Our study also shows that the unclassified variants are very rare (Table 2).

The limitation was that this study was not done on disease individuals whereby the incidence of variations associated with the disease population might be variable compared to a healthy population. Another

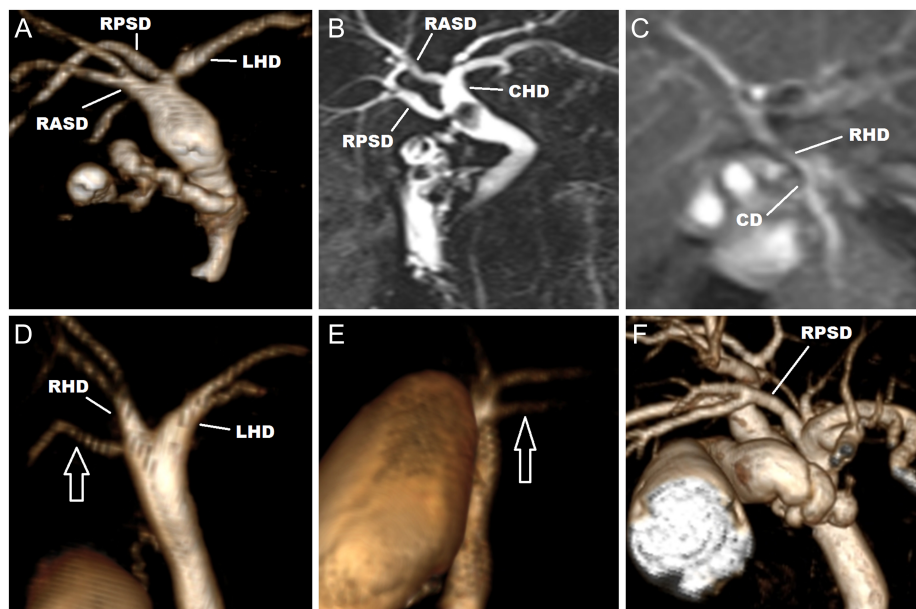


Figure 3. MRCP of variants of right hepatic duct insertion. (A) Volume rendered (VR) image showing right posterior sectoral duct (RPSD) joining LHD (type IIIA). (B) Thin slice T2-WI image showing RPSD joining common hepatic duct (CHD) (type IIIB). (C) Thin slice T2-WI showing the right hepatic duct (RHD) joining the cystic duct (CD) (type IV). (D) VR image showing accessory hepatic duct (open arrow) (type V). (E) Showing one of the left hepatic ducts (open arrow) joining the CHD (type VI). (F) Showing unclassified where the RPSD appear to join the confluence of the left hepatic ducts high inserted cystic duct (type VII). LHD, left hepatic duct; MRCP, magnetic resonance cholangiopancreatography.

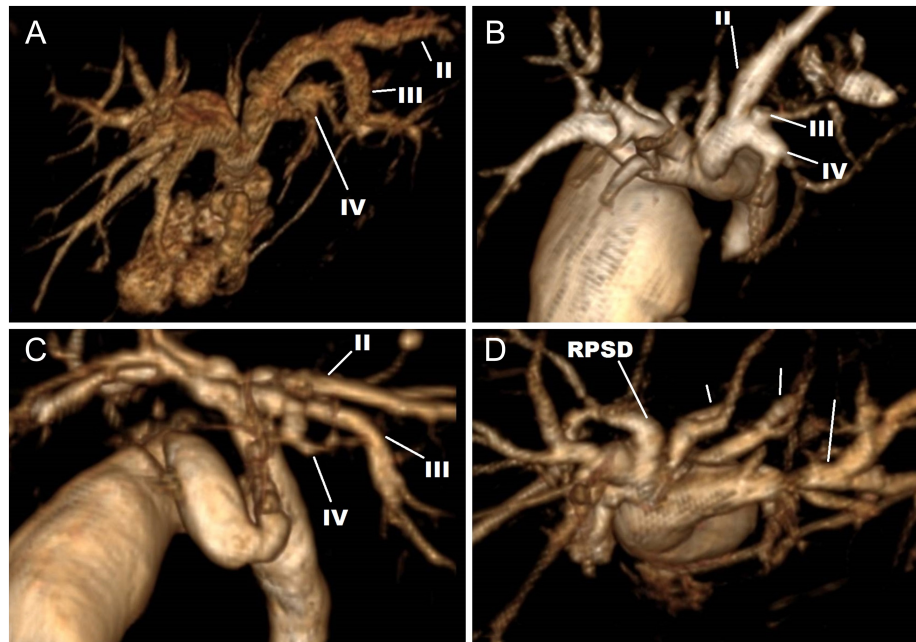


Figure 4. MRCP volume rendered images showing variants of left hepatic duct insertion. (A) The common trunk of segment II and III duct joins the segment IV duct to form the left hepatic duct. (B) Triconfluence of segment II, III, and IV. (C) Segment II joins the common trunk of segments III and IV. (D) Unclassified variant showing segments 3 ducts (white lines) from the left lobe independently draining to the CHD. CHD, common hepatic duct; MRCP, magnetic resonance cholangiopancreatography.

limitation is that we did not have any comparison with intraoperative cholangiography or ERCP. Also cases were included only if anatomy was clearly depicted, due to which many variants might have been together been excluded.

MRCP being an accurate, safe and non invasive imaging modality in hepatobiliary can outline common anatomical intrahepatic biliary variants which will serve as a preoperative roadmap for surgical and radiological hepatobiliary interventions. Medial insertion of the right posterior sectoral duct to the right anterior sectoral duct to form

the RHD is the most common drainage of the right lobe and common branch of segment II and III joining the segment IV is the most common left hepatic variant. This study also shows that visualizing a typical RHD insertion will reflect a possible typical LHD insertion in most cases.

Ethics Committee Approval: Ethics committee approval was received for this study from the ethics committee of North Eastern Indira Gandhi Regional Institute of Health and Medical Sciences (Date: July 2,2019, Number: NEIGR/IEC/M8/F12/19).

Informed Consent: Due to the retrospective design of the study, informed consent was not taken.

Peer-review: Externally peer-reviewed.

Author Contributions: Concept – D.L., P.R.; Design – D.L.; Supervision – D.L., C.D.; Resources – D.L.; Materials – D.L., P.R., P.K.; Data Collection and/or Processing – D.L., P.R., P.K.; Analysis and/or Interpretation – D.L., P.R., P.K.; Literature Search – D.L.; Writing Manuscript – D.L.; Critical Review – C.D.

Declaration of Interests: The authors have no conflicts of interest to declare.

Funding: The authors declared that this study has received no financial support.

REFERENCES

1. Sureka B, Bansal K, Patidar Y, Arora A. Magnetic resonance cholangiographic evaluation of intrahepatic and extrahepatic bile duct variations. *Indian J Radiol Imaging*. 2016;26(1):22-32. [\[CrossRef\]](#)
2. Sarawagi R, Sundar S, Raghuvarshi S, Gupta SK, Jayaraman G. Common and uncommon anatomical variants of intrahepatic bile ducts in magnetic resonance cholangiopancreatography and its clinical implication. *Pol J Radiol*. 2016;81:250-255. [\[CrossRef\]](#)
3. Choi JW, Kim TK, Kim KW, et al. Anatomic variation in intrahepatic bile ducts: an analysis of intraoperative cholangiograms in 300 consecutive donors for living donor liver transplantation. *Korean J Radiol*. 2003;4(2):85-90. [\[CrossRef\]](#)

Table 2. Variations in Intrahepatic Duct Anatomical Variations

	Our study, Lynser et al (n=347)	Choi et al. ³ 2003 (n=300)	Sarawagi et al. ² 2015 (n=224)	Gupta et al. ⁷ 2016 (n=458)
Typical finding	72%	63%	55.3%	65.72%
Anomalous RPSD to LHD	5.7%	11%	27.6%	14%
Triple confluence	17%	10%	9.3%	12.23%
RPSD to common hepatic duct	2.9%	6%	4%	4.4%
RPSD to cystic duct	-	2%	0.8%	0.4%
RHD to cystic duct	0.3%	0.3%	1.3%	-
Accessory duct to CHD/CBD	0.58%	5%	4.9%	0.7%
Accessory duct to RHD	-	-	-	0.2%
Individual drainage of LHD to RHD or CHD	0.86%	1%	-	0.2%
Unclassified	0.58%	1%	-	2.2%

CHD, common hepatic duct; LHD, left hepatic duct; RASD, right anterior sectoral duct; RHD, right hepatic duct; RPSD, right posterior sectoral duct; CBD, common bile duct.

4. Kitami M, Takase K, Murakami G, et al. Types and frequencies of biliary tract variations associated with a major portal venous anomaly: analysis with multi-detector row CT cholangiography. *Radiology*. 2006;238(1):156-166. [\[CrossRef\]](#)
5. Hyodo T, Kumano S, Kushihata F, et al. CT and MR cholangiography: advantages and pitfalls in perioperative evaluation of biliary tree. *Br J Radiol*. 2012;85(1015):887-896. [\[CrossRef\]](#)
6. Ragab A, Lopez-Soler RI, Oto A, Testa G. Correlation between 3DMRCP and intraoperative findings in right liver donors. *Hepatobiliary Surg Nutr*. 2013;2(1):7-13. [\[CrossRef\]](#)
7. Gupta A, Rai P, Singh V, Gupta RK, Saraswat VA. Intrahepatic biliary duct branching patterns, cystic duct anomalies, and pancreas divisum in a tertiary referral center: a magnetic resonance cholangiopancreatographic study. *Indian J Gastroenterol*. 2016;35(5):379-384. [\[CrossRef\]](#)
8. Cho A, Okazumi S, Yoshinaga Y, Ishikawa Y, Ryu M, Ochiai T. Relationship between left biliary duct system and left portal vein: evaluation with three-dimensional portocholangiography. *Radiology*. 2003;228(1):246-250. [\[CrossRef\]](#)
9. Ohkubo M, Nagino M, Kamiya J, et al. Surgical anatomy of the bile ducts at the hepatic hilum as applied to living donor liver transplantation. *Ann Surg*. 2004;239(1):82-86. [\[CrossRef\]](#)
10. Mortelé KJ, Ros PR. Anatomic variants of the biliary tree: MR cholangiographic findings and clinical applications. *AJR Am J Roentgenol*. 2001;177(2):389-394. [\[CrossRef\]](#)
11. Catalano OA, Singh AH, Uppot RN, Hahn PF, Ferrone CR, Sahani DV. Vascular and biliary variants in the liver: implications for liver surgery. *RadioGraphics*. 2008;28(2):359-378. [\[CrossRef\]](#)

Evaluation of Magnetic Resonance Imaging Findings of COVID-19-Related Rhino-Orbito-Cerebral Mucormycosis

Bişar Akbaş¹ , Bedir Kaya¹ , Ahsen Çavuşoğlu Akbaş² , Nazlı Nida Kaya³ , Ömer Kaya¹ ,
Figen Binokay¹ , Yunus Kenan Bıçakçı¹ 

¹Department of Radiology, Çukurova University, Faculty of Medicine, Adana, Turkey

²Department of Ophthalmology, Seyhan State Hospital, Adana, Turkey

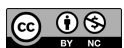
³Department of Medical Microbiology, Çukurova State Hospital, Adana, Turkey

Cite this article as: Akbaş B, Kaya B, Çavuşoğlu Akbaş A, et al. Evaluation of magnetic resonance imaging findings of COVID-19-related rhino-orbito-cerebral mucormycosis. *Current Research in MRI*, 2023;2(1):6-10.

Corresponding author: Ömer Kaya, e-mail: dr.omerkaya@gmail.com

Received: January 2, 2023 **Accepted:** February 14, 2023 **Publication Date:** March 25, 2023

DOI:10.5152/CurrResMRI.2023.22047



Content of this journal is licensed under a Creative Commons
Attribution-NonCommercial 4.0 International License.

Abstract

Objective: Rhino-orbito-cerebral mucormycosis is an angioinvasive, opportunistic infection in coronavirus disease 2019 patients. The aim of this study is to evaluate the spread and complications of coronavirus disease 2019-related rhino-orbito-cerebral mucormycosis with magnetic resonance imaging findings.

Methods: The study included 14 patients with head and neck magnetic resonance imaging, positive severe acute respiratory failure syndrome Coronavirus 2 (SARS-CoV-2) reverse transcriptase polymerase chain reaction test, and pathologically proven mucormycosis. Paranasal sinus, orbital and intracranial involvement features were examined in detail and complications were evaluated.

Results: Diabetes mellitus was the most common comorbidity in all patients except one (92%). Systemic steroid treatment was provided to 10 patients (74%) and oxygen support was provided to 8 patients (57%). In our study, the mortality rate was found to be 35%. Rhinosinusitis was the most common radiological finding present in all patients at the time of diagnosis. Orbital involvement was detected in 10 patients (71%) and intracranial involvement in 9 patients (64%).

Conclusion: Magnetic resonance imaging has an important role in diagnosing and determining complications and managing the disease in patients with coronavirus disease 2019-associated rhino-orbito-cerebral mucormycosis.

Keywords: COVID-19, mucormycosis, rhino-orbito-cerebral, MRI

INTRODUCTION

Mucormycosis is an infectious disease caused by fungi of the Mucorales group, showing an aggressive course with high morbidity and mortality rates and can be found commensal in the nasal cavity.^{1,2}

The novel coronavirus disease 2019 (COVID-19) may present with a broad clinical spectrum, ranging from mild symptoms to life-threatening pneumonia. In addition, the incidence of mucormycosis, which accompanies viral symptoms worldwide due to the COVID-19 pandemic, especially with the second wave, has attracted attention.^{3,4} Mucormycosis is a fungal infection that can be extremely mortal, particularly if it affects someone who has diabetes, uses steroids, or has a compromised immune system.^{5,6} In COVID-19-related cases, the pathophysiology has not been fully elucidated, but a marked decrease in CD4+T and CD8+T cell counts, uncontrolled diabetes, steroid therapy, and prolonged hospitalization are among possible risk factors.⁷

Mucormycosis can be colonized in the nasal mucosa and can lead to invasive infection in immunocompetent patients, and spreads directly to adjacent areas via the superior orbital fissure and cribriform plate, while vascular invasion occurs through the ophthalmic vessels, and intracranial involvement is in the carotid artery or perineural invasion.^{8,9} Rhino-orbito-cerebral mucormycosis (ROCM) is the most common mucormycosis involving the maxillofacial and orbital regions. It can spread intracranially in later stages and has a high mortality rate.¹⁰ The incidence of ROCM is increasing in the COVID-19 pandemic worldwide, especially in India, and this situation is met with concern by the authorities.^{11,12} The most common clinical findings are nasal congestion, rhinorrhea, facial swelling, facial and/or orbital pain, headache, proptosis, sudden vision loss, facial paresthesia and paralysis, sudden ptosis, diplopia, fever, and focal seizures.¹³ Rhino-orbito-cerebral mucormycosis is a fatal disease with a progressive course, delay in diagnosis or treatment can have devastating effects on patient survival.¹⁴ Early detection and treatment of mucormycosis can save lives, 1 week delay in treatment increases mortality from 35% to 66%.¹⁵ Both computed tomography (CT) and magnetic resonance imaging (MRI) play an important role in diagnosing ROCM. Magnetic resonance imaging is superior to CT in detecting complications such as acute cerebral ischemia, cerebritis, abscess, and vessel wall invasion.^{16,17}

This study aims to describe COVID-19-related ROCM imaging findings, cerebrovascular complications, and spread with imaging modalities.

METHODS

This study was conducted by retrospectively scanning the preoperative imaging findings of 14 patients who developed COVID-19-associated ROCM between September 2021 and February 2022 in Çukurova University Faculty of Medicine Hospital After the approval of the ethics committee dated December 2, 2022 and numbered 128. Patients with positive SARS-CoV-2 reverse transcriptase polymerase chain reaction (RT-PCR) test within 2 months were included in the study. All patients have pathological diagnosis and MR imaging.

Patients with primary malignancy, immunodeficiency, chemotherapy or radiotherapy were excluded from the study. Demographic data, comorbidities, all history and laboratory information regarding COVID-19 infection were collected. Two devices were used for MR examinations; 1.5 Tesla General Electric HDI ECHOSPEED (GE Healthcare, Milwaukee, USA) using an 8-channel head-neck coil, and Philips IntelliSpace Portal, Version 5.0, with a 16-channel head-neck coil (Philips Healthcare, Amsterdam, Netherlands). In addition to conventional MR sequences, diffusion-weighted imaging (DWI), axial and coronal fat-sat and mDIXON, time of flight (TOF) MR angiography, and post contrast 3DT1 were obtained for all patients. Post-contrast T1W images were acquired at 30 seconds after an injection of 0.1-mmol/kg gadobutrol (Gadovist; Bayer Schering Pharma AG, Germany). Radiological images were independently evaluated by 2 radiologists.

Paranasal sinus contents were evaluated by comparing with gray matter. The patients were evaluated in terms of orbital, retroantral region, masticator space, premaxillary/preseptal region involvement. Contrast-enhanced T1W and diffusion images were examined for infarction, black turbinate sign, dural contrast, cerebritis, intracranial abscess, perineural invasion, and orbital and intracranial spread pathways of infection. Vascular invasion/occlusion was evaluated with MR angiography sequences.

RESULTS

The gender distribution of the 14 patients included in the study consisted of an equal number of men and women. The mean age was 58.7 (15-82). The median time from RT-PCR test positivity at the time of diagnosis was 17 days (min: 1-max: 59). Diabetes mellitus (DM) was the most common comorbid 13 (92%) comorbid diseases, and the mean HbA1c was found to be 8.4%. All of the patients were followed up with hospitalization; Systemic steroid therapy was provided to 10 patients (74%), and oxygen support was provided to 8 patients (57%). 5 patients (35%) died during follow-up.

Rhinosinusitis was present at the time of diagnosis in all patients and was the most common radiological finding. Maxillary and ethmoid sinuses were the most frequently involved paranasal sinuses. Orbital involvement was the second most common finding, seen in 10 patients (71%). Post-contrast images showed a loss of contrast enhancement

Table 1. Radiologic Imaging Findings in Patients Who Developed COVID-19-Associated Rhino-Orbito-Cerebral Mucormycosis

Imaging Findings	Number (%)
Paranasal sinus involvement	14 (100)
Orbital involvement	10 (71)
Cavernous sinus involvement	6 (42)
Pterygopalatine fossa involvement	8 (57)
Perineural spread	4 (28)
Pachymeningeal enhancement/involvement	8 (57)
Subdural abscess	4 (28)
Cerebritis	2 (14)
Unilateral ICA occlusion	4 (28)
Acute cerebral infarction	3 (21)

COVID-19, coronavirus disease 2019.

in the nasal mucosa defined as 'black turbinate' in 9 patients (64%). Cavernous sinus involvement in 6 patients (42%), pterygopalatine fossa involvement and pachymeningeal enhancement in 8 patients (57%), perineural spread in 4 patients (28%) (3 patient with 5th cranial nerve and one patient with 7th cranial nerve involvement), subdural abscess and unilateral internal carotid artery (ICA) occlusion in 4 patients (28%), cerebral infarction in 3 patients (21%), and cerebritis in 2 patients (14%) were detected. Mandibular osteomyelitis developed in one patient due to temporomandibular joint involvement, and osteomyelitis of the frontal bone developed in another patient. Table 1 shows radiological involvement areas.

DISCUSSION

Rhino-orbito-cerebral mucormycosis is the most common variant of mucormycosis infection.¹⁸ Rhino-orbito-cerebral mucormycosis has a fulminant course and shows a similarly high mortality in our study as stated in the literature.¹⁹ Limited sinonasal disease is a broad term denoting rhino-orbital disease and/or rhino-orbital-cerebral disease. The disease is mainly manifested by facial swelling, headache, decreased vision, and fever.

Due to the immune dysregulation that develops in COVID-19, patients become more prone to develop secondary infections.²⁰ In line with the results we obtained from our research, the most common comorbidity encountered in the development of mucormycosis infection is diabetes mellitus.²¹ In addition, high-dose corticosteroids, which are widely used in the treatment of COVID-19, cause immunosuppression by inhibiting the sequestration of CD4+T lymphocytes and the transcription of cytokines in the reticuloendothelial system.²²

Sino-nasal involvement was the most common finding in all patients at the time of diagnosis. 'Black turbinate' represents post-contrast signal loss due to microvascular angioinvasion of the nasal mucosa and consequent necrosis (Figure 1). Orbital involvement presents as intense inflammation in the pre- and/or post-septal distance, effacement in adipose tissue planes, proptosis, increased signal in extraocular muscles, and enhancement. Diffusion restriction in the optic nerve develops as a result of ophthalmic artery invasion and causes permanent vision loss (Figure 1 and 2). The 'Guitar Pick' sign is used to define the conical deformation of the eyeball as a result of increased intraorbital pressure (Figure 1).

Intracranial involvement is the most dangerous and mortality-related complication. Although intracranial spread can occur in several ways, the majority of cases are the primary entry localization of the

MAIN POINTS

- Rhino-orbito-cerebral mucormycosis is an angioinvasive and opportunistic infection.
- Its frequency and aggressiveness increase with SARS-CoV-2.
- Magnetic resonance imaging has an important role in diagnosing and determining complications and managing the disease.

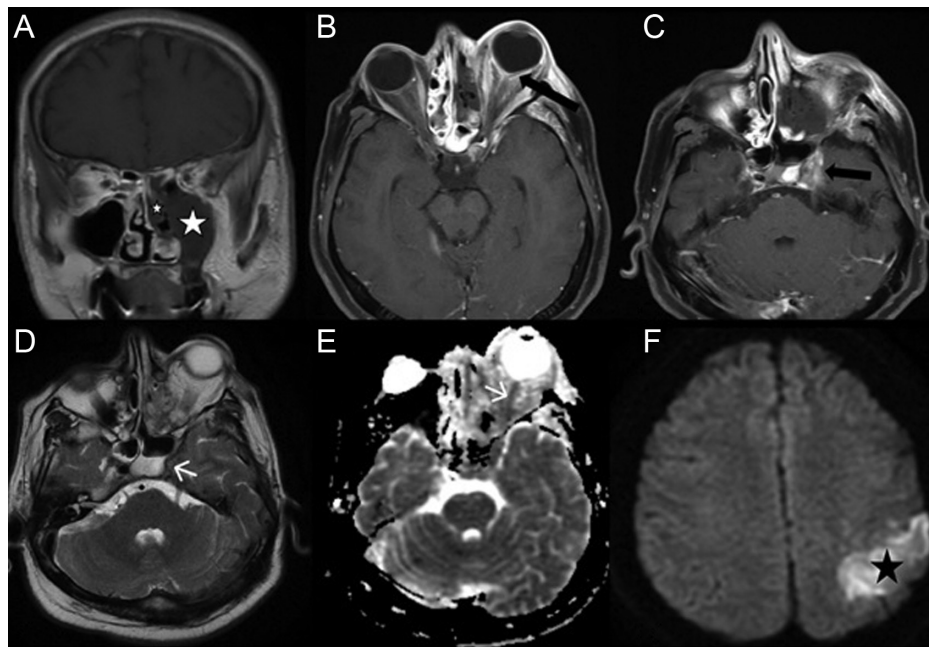


Figure 1. A 33-year-old male presented with swelling and pain in the left eye on the 13th day post-COVID. Coronal post-contrast T1W image (A) show the 'black turbinate sign' of the left middle nasal concha without contrast and the mucosa of the left maxillary sinus (white stars). Axial post-contrast T1W (B, C) images show 'guitar pick sign' and orbital fat tissue involvement due to conical posterior ocular deformation on the left, abnormal contrast enhancement in the left cavernous sinus wall and adjacent dura, absence of contrast enhancement due to occlusion in the left ICA (thick black arrow). Flow void detected due to occlusion in the left ICA on axial T2W image (D) (white arrow). ADC images (E) show hypointensity (white arrow) due to left optic nerve infarction. Diffusion-weighted imaging image (F) show diffusion restriction due to infarction in the left parietal lobe (black star).

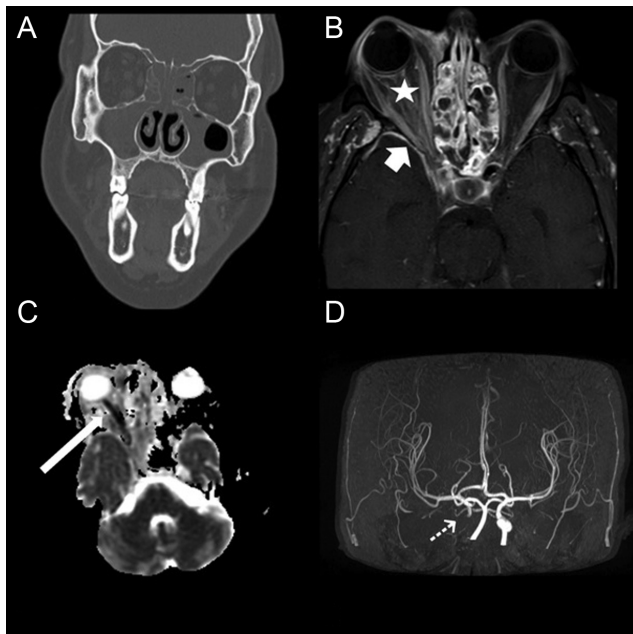


Figure 2. A 50-year-old man applied for vision loss and swelling in the right eye on the 9th day of COVID positivity. Coronal bone window CT image (A) shows intense opacification in the paranasal sinuses. Axial post-contrast T1W image (B) shows contrast enhancement (star) secondary to involvement in the right orbital fat tissue, proptosis, and anterior temporal dural enhancement (short arrow). ADC image (C) shows signal loss secondary to right optic nerve infarction (long arrow) and MR angiography (D) shows terminal blunt termination due to right ICA occlusion (dashed arrow). Although the patient had right ICA occlusion, no infarct finding was observed because the communicating arteries were patent.

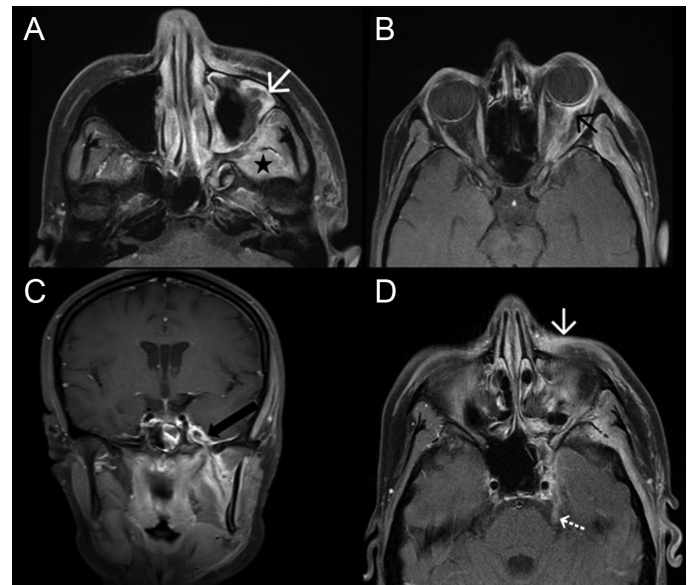


Figure 3. A 15-year-old girl with type 1 diabetes and celiac disease received steroid treatment on the 14th day of COVID positivity and applied to the hospital with a complaint of swelling in the left eye. Axial post-contrast T1W images (A, B, D) show thickening and contrast enhancement in the left maxillary sinus mucosa and periantral soft tissue (white arrow). Contrast enhancement and proptosis (black arrow) secondary to involvement in the left retroorbital fat tissue and optic nerve, thickening and enhancement (dashed arrow) representing perineural invasion in the left trigeminal nerve ganglion are observed. Coronal T1W post-contrast image (C) show contrast enhancement due to inflammation in the left masticator space, intense inflammation extending to the cavernous sinus through the foramen ovale, and a subdural abscess adjacent to the cavernous sinus (thick black arrow).

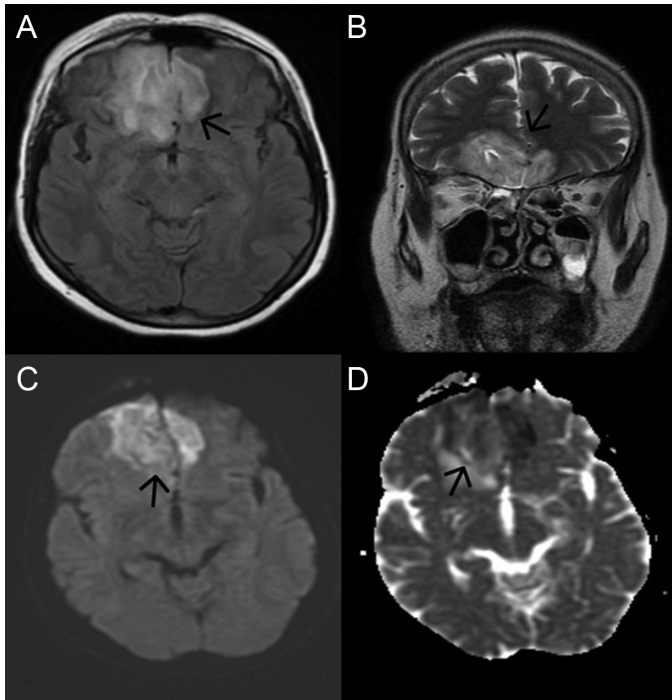


Figure 4. A 61-year-old woman applied with a complaint of limitation in right eye movements on the 20th day of COVID positivity. In axial T2 FLAIR (A) and coronal T2W (B) images, there is intense signal increase in the right wider bifrontal basal areas and right middle frontal part. Diffusion-weighted imaging (C) and ADC (D) images show diffusion restriction secondary to cerebritis (arrows).

pterygopalatine fossa. In our study, the most common form of intracranial involvement was cavernous sinus involvement (Figure 1 and 3). Occlusion (Figure 1 and 2), perineural invasion (Figure 3), subdural abscess (Figure 3) and cerebritis (Figure 4) as a result of internal carotid artery (ICA) angioinvasion are other intracranial complications developed in our patient population. Vascular involvement, characterized by thrombosis and tissue necrosis, is the pathological hallmark of mucormycosis.²³ The presence of high amounts of free iron in tissues and blood is believed to play an important role in the pathogenesis of vascular invasion. Mucormycosis may form a mucorthrombus in the form of vasculitis or directly in the vessel lumen.²⁴ Four of our patients had unilateral ICA occlusion, but none of them developed pseudoaneurysm formation.

The majority of case reports, series, and original articles in the literature have been based on data from the Indian patient population. In this respect, our study presents the most comprehensive study in Turkey in terms of the number of patients it includes. In addition, we have not come across any single-center study from Europe with such a large number of cases in the literature.

Mucormycosis infection should be kept in mind especially in cases such as concomitant diabetes, immunosuppression and prolonged hospitalization. Some studies suggest that patients with COVID-19 disease and at risk should be followed closely from the 10th day to the 6th week, when they are most vulnerable to mucor infection, and that screening imaging should be performed.

The limitations of the study include the small sample size, the fact that it is a single-center retrospective study, and the inability to demonstrate

radiological and clinical differences between mucor infection developing in patients with COVID-19 and unrelated COVID-19 mucor infection.

As a conclusion, radiologists should be aware of the diagnosis and complication imaging findings due to the high incidence of rhino-orbito-cerebral mucormycosis in the COVID-19 pandemic. Mucor infection, which is rare but mortal, should be kept in mind in patients with active or recovering COVID-19, especially those with concomitant diabetes and those receiving long-term steroid therapy, and MR imaging should be performed without delay, especially in determining intracranial complications and the spread of the disease.

Ethics Committee Approval: Ethics committee approval was received for this study from the ethics committee of Çukurova University (Date: December 2, 2022, Number: 128).

Informed Consent: Written informed consent was not obtained from the patients whose MRI images were included in this study, since the study was performed with radiological images only.

Peer-review: Externally peer-reviewed.

Author Contributions: Concept – Ö.K., Y.K.B.; Design – Ö.K., B.A.; Supervision – Ö.K., F.B., Y.K.B.; Resources – B.A., B.K.; Materials – B.A., B.K., Ö.K.; Data Collection and/or Processing – B.A., Ö.K.; Analysis and/or Interpretation – B.A., Ö.K.; Literature Search – B.A., A.Ç.A., N.N.K.; Writing Manuscript – B.A., Ö.K.; Critical Review – Ö.K.

Declaration of Interests: The authors declare that they have no competing interest.

Funding: The authors declared that this study has received no financial support.

REFERENCES

1. Danion F, Aguilar C, Catherinot E, et al. Mucormycosis: new developments into a persistently devastating infection. *Semin Respir Crit Care Med.* 2015;36(5):692-705. [\[CrossRef\]](#)
2. Limon JJ, Skalski JH, Underhill DM. Commensal fungi in health and disease. *Cell Host Microbe.* 2017;22(2):156-165. [\[CrossRef\]](#)
3. Sen M, Lahane S, Lahane TP, Parekh R, Honavar SG. Mucor in a viral land: a tale of two pathogens. *Indian J Ophthalmol.* 2021;69(2):244-252. [\[CrossRef\]](#)
4. Ravani SA, Agrawal GA, Leuva PA, Modi PH, Amin KD. Rise of the phoenix: mucormycosis in COVID-19 times. *Indian J Ophthalmol.* 2021;69(6):1563-1568. [\[CrossRef\]](#)
5. Seaton RA, Gibbons CL, Cooper L, et al. Survey of antibiotic and antifungal prescribing in patients with suspected and confirmed COVID-19 in Scottish hospitals. *J Infect.* 2020;81(6):952-960. [\[CrossRef\]](#)
6. Skiada A, Pavleas I, Drogari-Apiranthitou M. Epidemiology and diagnosis of mucormycosis: an update. *J Fungi (Basel).* 2020;6(4):265. [\[CrossRef\]](#)
7. Pemán J, Ruiz-Gaitán A, García-Vidal C, et al. Fungal co-infection in COVID-19 patients: should we be concerned? *Rev Iberoam Micol.* 2020;37(2):41-46. [\[CrossRef\]](#)
8. Spellberg B, Edwards Jr J, Ibrahim A. Novel perspectives on mucormycosis: pathophysiology, presentation, and management [presentation]. *Clin Microbiol Rev.* 2005;18(3):556-569. [\[CrossRef\]](#)
9. Parsi K, Itgampalli RK, Vittal R, Kumar A. Perineural spread of rhino-orbitocerebral mucormycosis caused by *Apophysomyces elegans*. *Ann Indian Acad Neurol.* 2013;16(3):414-417. [\[CrossRef\]](#)
10. Song G, Liang G, Liu W. Fungal co-infections associated with global COVID-19 pandemic: a clinical and diagnostic perspective from China. *Mycopathologia.* 2020;185(4):599-606. [\[CrossRef\]](#)
11. Sarkar S, Gokhale T, Choudhury SS, Deb AK. COVID-19 and orbital mucormycosis. *Indian J Ophthalmol.* 2021;69(4):1002-1004. [\[CrossRef\]](#)
12. Honavar SG. Code mucor: guidelines for the diagnosis, staging and management of rhino-orbito-cerebral mucormycosis in the setting of COVID-19. *Indian J Ophthalmol.* 2021;69(6):1361-1365. [\[CrossRef\]](#)
13. Deepalam S, Siddiqui A, et al. Coronavirus Disease 2019 (COVID-19)–Associated Rhino-Orbito-Cerebral Mucormycosis: a Multi-Institutional Retrospective Study of Imaging Patterns. *World Neurosurg* 2022;162:131-140.

14. Cornely OA, Alastruey-Izquierdo A, Arenz D, et al. Global guideline for the diagnosis and management of mucormycosis: an initiative of the European Confederation of Medical Mycology in cooperation with the Mycoses Study Group Education and Research Consortium. *Lancet Infect Dis.* 2019;19(12):e405-e421. [\[CrossRef\]](#)
15. Werthman-Ehrenreich A. Mucormycosis with orbital compartment syndrome in a patient with COVID-19. *Am J Emerg Med.* 2021;42:264.e5-264.e8. [\[CrossRef\]](#)
16. Wani N, Jehangir M, Lone P. Rhino-orbito-cerebral mucormycosis: magnetic resonance imaging. *Indian J Otol.* 2015;21(3):215. [\[CrossRef\]](#)
17. Herrera DA, Dublin AB, Ormsby EL, Aminpour S, Howell LP. Imaging findings of rhinocerebral mucormycosis. *Skull Base.* 2009;19(2):117-125. [\[CrossRef\]](#)
18. Jeong W, Keighley C, Wolfe R, et al. The epidemiology and clinical manifestations of mucormycosis: a systematic review and meta-analysis of case reports. *Clin Microbiol Infect.* 2019;25(1):26-34. [\[CrossRef\]](#)
19. Prakash H, Chakrabarti A. Epidemiology of mucormycosis in India. *Microorganisms.* 2021;9(3):523. [\[CrossRef\]](#)
20. Chakrabarti SS, Kaur U, Aggarwal SK, et al. The pathogenetic dilemma of post-COVID-19 mucormycosis in India. *Aging Dis.* 2022;13(1):24-28. [\[CrossRef\]](#)
21. Bhansali A, Bhadada S, Sharma A, et al. Presentation and outcome of rhino-orbital-cerebral mucormycosis in patients with diabetes. *Postgrad Med J.* 2004;80(949):670-674. [\[CrossRef\]](#)
22. Barshes NR, Goodpastor SE, Goss JA. Pharmacologic immunosuppression. *Front Biosci.* 2004;9(1):411-420. [\[CrossRef\]](#)
23. Morace G, Borghi E. Invasive mold infections: virulence and pathogenesis of mucorales. *Int J Microbiol.* 2012;2012:349278. [\[CrossRef\]](#)
24. Kumar H M, Sharma P, Rudramurthy SM, et al. Serum iron indices in COVID-19-associated mucormycosis: a case-control study. *Mycoses.* 2022;6 (1):120-127. [\[CrossRef\]](#)

The Relationship Between Patellar Chondromalacia and Patellofemoral Joint Anatomical Variations

Can Usal¹, Atilla Hikmet Çilengir¹, Orkun Sarıoğlu¹, Berna Dirim Mete¹, Özgür Tosun²

¹İzmir Democracy University, Buca Seyfi Demirsoy Training and Research Hospital, İzmir, Turkey

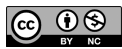
²İzmir Katip Çelebi University, Atatürk Training and Research Hospital, İzmir, Turkey

Cite this article as: Usal C, Çilengir AH, Sarıoğlu O, Dirim Mete B, Tosun Ö. The relationship between patellar chondromalacia and patellofemoral joint anatomical variations. *Current Research in MRI*, 2023;2(1):11-15.

Corresponding author: Can Usal, e-mail: canusal@gmail.com

Received: January 19, 2023 **Accepted:** February 22, 2023 **Publication Date:** April 7, 2023

DOI:10.5152/CurrResMRI.2023.22044



Content of this journal is licensed under a Creative Commons Attribution-NonCommercial 4.0 International License.

Abstract

Objective: To analyze the relationship between lateral patellar tilt angle, lateral patella-femoral angle, patella–patellar tendon angle, and lateral trochlear inclination angle.

Methods: Cases with knee magnetic resonance imaging between June and October 2022 were analyzed retrospectively. Two groups of 50 each with and without patella chondromalacia were formed. lateral patellar tilt angle, lateral patella-femoral angle, patella–patellar tendon angle, and lateral trochlear inclination angle values were measured on the knee magnetic resonance imaging. Chondromalacia was evaluated and graded. The differences in age, gender, and measurement variables between the groups chondromalacia were analyzed.

Results: There were 58 women and 42 men. Seventeen (34%) patients had low-grade and 33 (66%) patients had high-grade chondromalacia. The median age was 49 (interquartile range: 61) in the chondromalacia group and 37.5 (interquartile range: 38) in the normal group ($P < .001$). The median lateral patellar tilt angle was 6.76 (interquartile range: 15.15) in the chondromalacia group and 6.92 (interquartile range: 19.25) in the normal group ($P = .610$). The median lateral patella-femoral angle was 7.86 (interquartile range: 41.86) in the chondromalacia group and 7.90 (interquartile range: 17.37) in the normal group ($P = 0.471$). Median patella–patellar tendon angle was 142.96 (interquartile range: 32.14) in the chondromalacia group and 145.87 (interquartile range: 27.77) in the normal group ($P = .006$). The median lateral trochlear inclination angle was 19.11 (interquartile range: 19.30) in the chondromalacia group and 20.39 (interquartile range: 20.16) in the normal group ($P = .127$).

Conclusion: The knee joint morphological variations may differ in between the groups with and without patellar chondromalacia. Older age and lower patella–patellar tendon angle were more frequent in the patellar chondromalacia group.

Keywords: anatomic variation, chondromalacia, knee, magnetic resonance imaging, patella

INTRODUCTION

The knee joint consists of the tibiofemoral and patellofemoral (PF) joints. Several soft tissue structures such as collateral ligaments, cruciate ligaments, patellar retinaculum, and menisci support their stability due to the articulation of anatomically incompatible bones. The diversity of these structures gives rise to morphological variations that are different in each person. These variations may be the cause of various pathologies in the knee, mostly in the PF joint.¹

One of the most common pathologies of the PF joint and an important cause of knee pain is patellar chondromalacia. Magnetic resonance imaging (MRI) is successful in assessing cartilage status with its high contrast resolution.¹ The presence of patellar chondromalacia can be detected and graded with MRI. It has been shown that anatomical variations in the PF joint can be successfully measured with MRI.² The lateral patellar tilt angle (LPTA), lateral patella-femoral angle (LPFA), patella–patellar tendon angle (PPTA), and lateral trochlear inclination angle (LTI) are the most important anatomical measurements in the PF joint. The relationship of each of them with patellar chondromalacia was examined in separate studies, and different results were obtained.²⁻⁶ However, the number of studies evaluating the relationship between these measurements and patellar chondromalacia is not sufficient.

Therefore, we hypothesized that anatomical variations involving the PF joint are associated with patellar chondromalacia. With this hypothesis, we aimed to analyze the relationship between patellar chondromalacia and LPTA, LPFA, PPTA, and LTI.

METHODS

The İzmir Democracy University Buca Seyfi Demirsoy Training and Research Hospital Ethics Committee approved this study and waived the requirement for informed consent (Date: December 28, 2022, No.:2022/12-124). Cases who underwent knee MRI for any reason between June and October 2022 were analyzed retrospectively. Between these dates, a total of 100 cases, 50 with and 50 without patellar chondromalacia, were

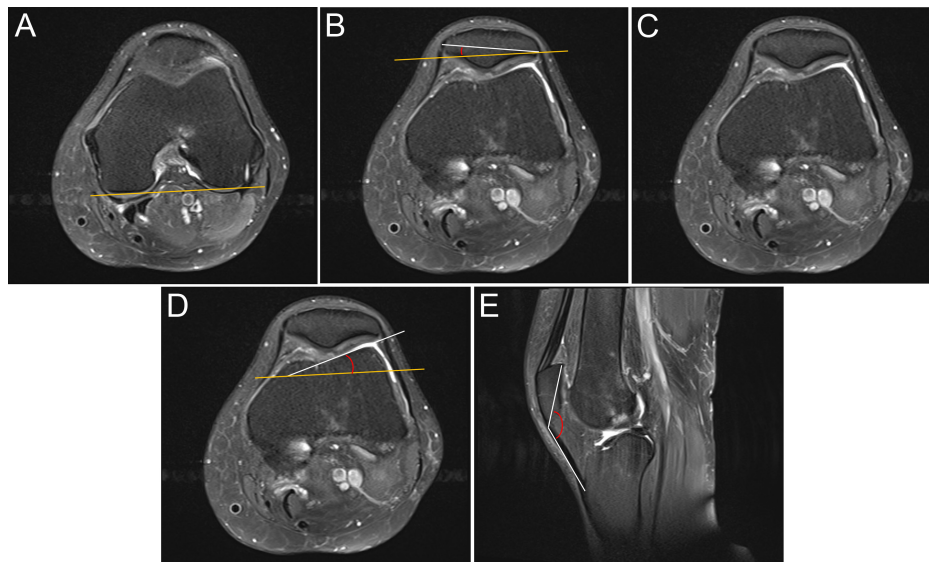


Figure 1. Patellofemoral joint anatomical variations. (A) The line tangent to the posterior femoral condyles. (B) The lateral patellar tilt angle between the line tangent to the subchondral bone in the posterior femoral condyle and the line forming the transverse axis of the patella. (C) The lateral patellofemoral angle is the angle between the line parallel to the tip of the anterior condyles and the lateral patellar facet. (D) The lateral trochlear inclination is the angle between the line tangent to the subchondral bone in the posterior femoral condyle and the line drawn parallel to the lateral trochlear facet subchondral bone. (E) The patella–patellar tendon angle is the angle between the line connects of the upper and lower poles of the patella and the line connects of the lower pole of the patella and the tibial tuberosity.

included in the study. Cases with a history of knee surgery, arthroscopy, moderate- or high-grade joint degeneration (e.g., Kellgren–Lawrence types 3 and 4), ligament/meniscus tear, joint effusion, and high-energy trauma were excluded ($n=32$). Since the etiology of ligament and meniscal tears and patellar chondromalacia may be similar (e.g., osteoarthritis), it is aimed to exclude factors other than anatomical variation and to be limited to ligament and meniscal tears in the etiology of patellar chondromalacia.

Magnetic resonance imaging was performed with 1.5T scanner (Magnetom Altea, Siemens Healthcare, Erlangen, Germany). The MRI protocol included fat-suppressed proton density sequence (coronal, axial, and sagittal) and T1-weighted sequence (coronal). The LPTA, LPFA, PPTA, and LTI values were measured on the knee MRIs of the patients (Figure 1). Chondromalacia was evaluated according to the modified Outerbridge classification.⁷ Cases with grades 1 and 2 chondromalacia were included to the low-grade subgroup, the cases with grades 3 and 4 were chondromalacia were included to the high-grade chondromalacia subgroup (Figure 2, Table 1).

The LPTA was measured on axial slices. The angle between the line tangent to the posterior femoral condyles and the transverse axis of the patella was considered as LPTA. As described in the literature,² for the transverse axis of the patella, the axial slice where the patella appears to be the widest, and for the line that is tangent to the posterior of

the femoral condyles, the axial slice where the condyles have the most posterior extension was selected. The angle between the line tangent to the posterior femoral condyles and the line drawn parallel to the lateral trochlear facet were considered as the LTI. The LPFA was measured between the line tangent to the tip of the anterior femoral condyles and the lateral patellar facet. The PPTA was measured between the line connects of the upper and lower points of the patella and the line connects of the lower point of the patella and the tibial tuberosity. The PPTA measurement was performed on the midsagittal slice.

Statistical analysis was done with IBM SPSS Statistics version 25.0 software (Armonk, NY, USA). Since our study population does not have a normal distribution, the difference in age and measurement variables between the groups with and without chondromalacia were examined with the Mann–Whitney *U*-test. The difference in gender

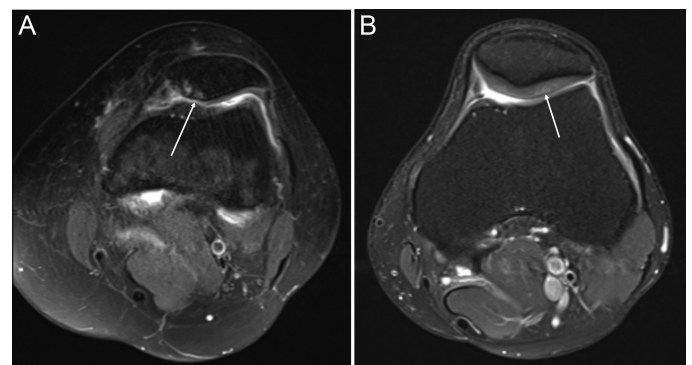


Figure 2. Two different axial fat-suppressed proton density images patients with high-grade chondromalacia (A) and low-grade chondromalacia (B). In Figure 2A, near-full-thickness cartilage loss (arrow) with underlying bone reactive changes is consistent with high-grade chondromalacia. In Figure 2B, focal areas of hyperintensity (arrow) without fraying/ or cartilage loss is seen.

MAIN POINTS

- Magnetic resonance imaging can be used for evaluating the knee joint anatomical variations.
- The patella–patellar tendon angle is lower, and age is higher in the patients with patellar chondromalacia.
- Anatomical variations can cause patellar chondromalacia.

Table 1. Modified Outerbridge Classification for MRI

Grade	MRI Findings
1	Focal areas of hyperintensity with normal contour
2	Blister-like swelling/fraying of articular cartilage extending to surface
3	Partial-thickness cartilage loss with focal ulceration
4	Full-thickness cartilage loss with underlying bone reactive changes

MRI, magnetic resonance imaging.

between the normal and chondromalacia groups was evaluated with the continuity corrected chi-square test. The distribution of parameters in the groups was given as median and interquartile range (IQR). A value of $P < .05$ was accepted as statistically significant.

RESULTS

The median age of the patients included in the study was 45 (IQR: 18.5). There were 58 women and 42 men. The median age was 49 (IQR: 61) in the group with patellar chondromalacia and 37.5 (IQR: 38) in the normal patellar cartilage group ($P < .001$). There was no statistically significant difference in gender distribution between the groups with patellar chondromalacia (25 females and 25 males) and those without (33 females and 17 males) ($P = .156$).

The median LPTA was 6.76 (IQR: 15.15) in the chondromalacia group and 6.92 (IQR: 19.25) in the normal patellar cartilage group ($P = .610$). The median LPFA was 7.86 (IQR: 41.86) in the chondromalacia group and 7.90 (IQR: 17.37) in the normal patellar cartilage group ($P = .471$). Median PPTA was 142.96 (IQR: 32.14) in the chondromalacia group and 145.87 (IQR: 27.77) in the normal patellar cartilage group ($P = .006$). The median LTI was 19.11 (IQR: 19.30) in the

chondromalacia group and 20.39 (IQR: 20.16) in the normal patellar cartilage group ($P = .127$).

In the patellar chondromalacia group, 17 (34%) patients had low-grade chondromalacia and 33 (66%) patients had high-grade chondromalacia. The median age was 42 (IQR: 20.5) in the low-grade patellar chondromalacia group and 52 (IQR: 17.5) in the high-grade patellar chondromalacia group ($P = .005$). There were 11 women (65%) and 6 men (35%) in the low-grade chondromalacia group, and 22 women (66.7%) and 11 men (33.3%) in the high-grade chondromalacia group ($P < .001$). The median LPTA was 6.21 (IQR: 6.43) in the low-grade patellar chondromalacia group and 7.19 (IQR: 5.4) in the high-grade patellar chondromalacia group ($P = .384$). The median LPFA was 6.93 (IQR: 8.94) in the low-grade patellar chondromalacia group and 8.1 (IQR: 8.67) in the high-grade patellar chondromalacia group ($P = .224$). Median PPTA was 143.16 (IQR: 8.64) in the low-grade patellar chondromalacia group and 142.76 (IQR: 7.37) in the high-grade patellar chondromalacia group ($P = .467$). The median LTI was 16.45 (IQR: 5.33) in the low-grade patellar chondromalacia group and 19.47 (IQR: 8.2) in the high-grade patellar chondromalacia group ($P = .407$).

Table 2 and Figure 3 summarize the results of the groups with and without chondromalacia, and Table 3 and Figure 4 summarize the results of the groups of high-grade and low-grade patellar chondromalacia.

DISCUSSION

The PF joint helps the quadriceps muscle to extend the knee with less force and is an essential component of the extensor mechanism. The load on the knee joint is distributed more homogeneously during extension with the PF joint. It has been described that anatomical

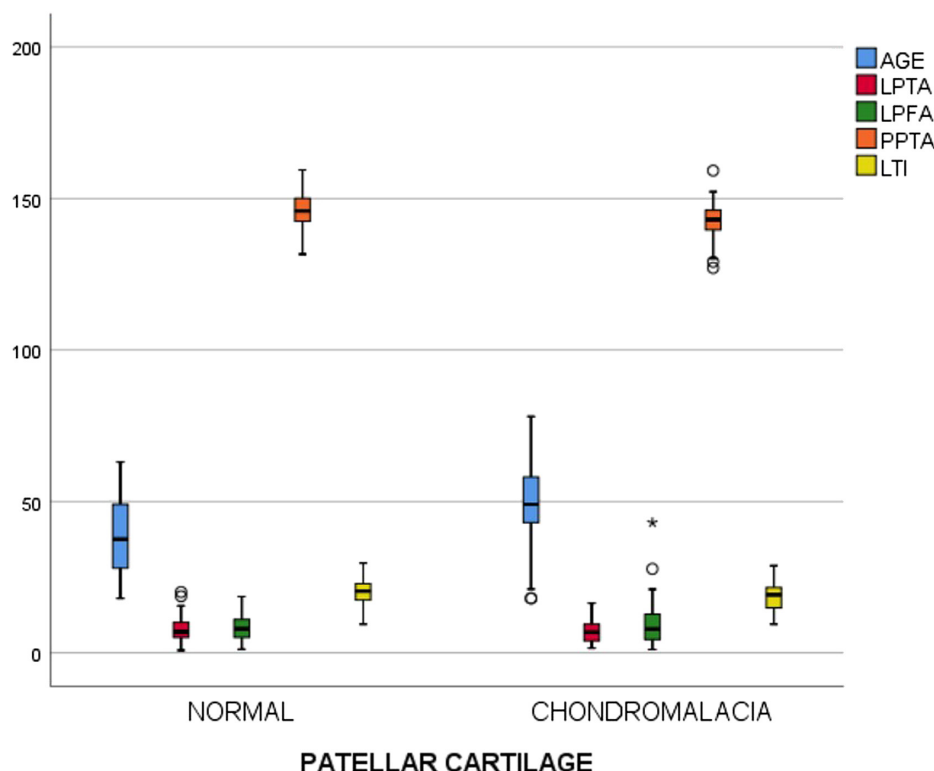
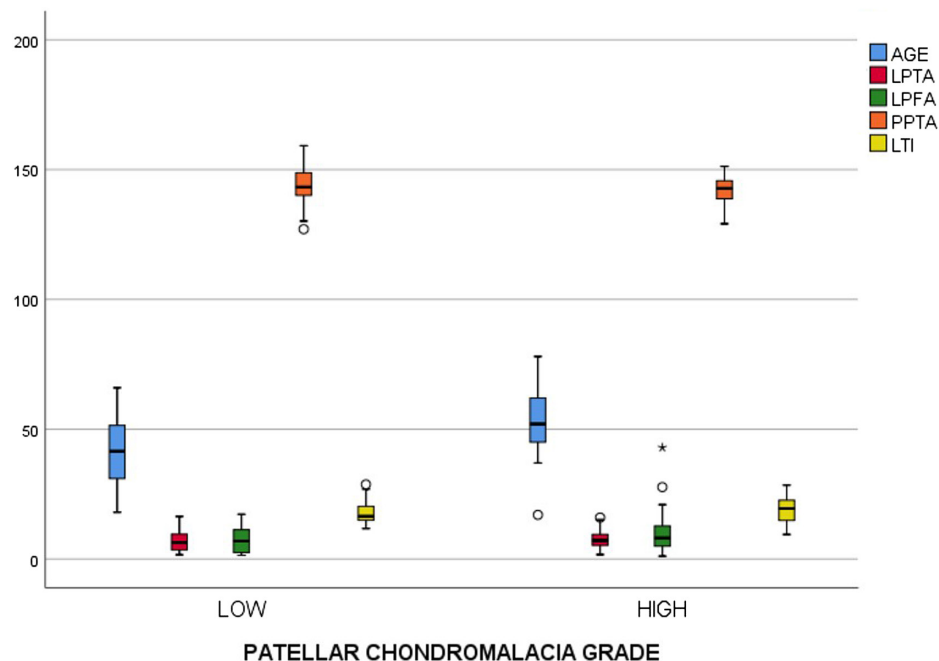


Figure 3. Box blot analyses of age and anatomical measurements between groups with and without patellar chondromalacia. LPFA, lateral patella-femoral angle; LPTA, lateral patellar tilt angle; LTI, lateral trochlear inclination angle; PPTA, patella–patellar tendon angle.

Table 2. Results of the Normal Patellar Cartilage Group and Patellar Chondromalacia Group

	Normal Group, median (Minimum–Maximum)	Chondromalacia Group, median (Minimum–Maximum)	P
Age (years)	37.5 (18-63)	49 (18-78)	< .001
Lateral patellar tilt angle	6.92 (0.82-20.07)	6.76 (1.25-16.4)	= .610
Lateral patellofemoral angle	7.90 (1.2-18.57)	7.86 (1.11-42.97)	= .471
Patella patellar tendon angle	145.87 (131.66-159.43)	142.96 (127.08-159.2)	= .006
Lateral trochlear inclination angle	20.39 (9.46-29.62)	19.11 (9.45-28.75)	= .127

**Figure 4.** Box blot analyzes of age and anatomical measurements between groups low-grade and high-grade patellar chondromalacia. LPFA, lateral patella-femoral angle; LPTA, lateral patellar tilt angle; LTI, lateral trochlear inclination angle; PPTA, patella–patellar tendon angle.

differences in the PF joint can cause damage to the patellar cartilage by affecting the load distribution.²⁻⁶ In this study, we aimed to reveal whether anatomical variations affect the patellar cartilage. We found a significant difference between the patellar chondromalacia and normal patellar cartilage groups in terms of PPTA. Other anatomical variations examined did not differ significantly between the 2 groups. The patellar chondromalacia group was significantly older than the normal patellar cartilage group. In addition, patients with high-grade chondromalacia in the patellar chondromalacia group were found to be significantly older than those with low grade.

The LPTA describes the lateral angulation of the patella in the axial plane.⁸ It causes anterior knee pain by causing patellar chondromalacia or fat-pad edema in some cases.²⁻⁶ We think that the LPTA is generally ignored in daily practice. In our study, we did not find a significant difference for LPTA between groups with and without patellar

chondromalacia. We did not evaluate fat-pad edema because it was not the aim of our study, but there are studies in the literature showing a significant relationship between increased LPTA, knee joint fat-pad edema, and anterior knee pain.^{2,9-11}

We found a significant difference between the groups with and without patellar chondromalacia in terms of median PPTA and median age. These results are compatible with other data in the literature. The fact that the patellar chondromalacia group was older than the normal group may have been due to degenerative cartilage changes. Although we exclude moderate-severe degeneration cases, degenerative chondromalacia that develops with age might have affected our results. Similarly, Gürsoy et al⁴ found the mean age to be significantly higher in the patellar chondromalacia group. We found lower values of PPTA in the patellar chondromalacia group. The angular position of the patella in the sagittal plane may have increased the load on the PF joint, leading to

Table 3. Results of the Low-Grade and High-Grade Patellar Chondromalacia Groups

	Low-Grade Chondromalacia, median (Minimum–Maximum)	High-Grade Chondromalacia, median (Minimum–Maximum)	P
Age (years)	42 (18-66)	52 (18-78)	= .005
Lateral patellar tilt angle	6.21 (1.25-16.4)	7.19 (1.68-15.96)	= .384
Lateral patellofemoral angle	6.93 (1.44-17.19)	8.1 (1.11-42.97)	= .224
Patella–patellar tendon angle	143.16 (127.08-159.2)	142.76 (129.1-151.2)	= .467
Lateral trochlear inclination angle	16.45 (11.7-28.75)	19.47 (9.45-28.46)	= .407

cartilage damage. Damgacı et al¹² and Kim et al¹³ found the mean PPTA significantly lower in the patients with patellar chondromalacia.

There was no significant difference between the groups for LPTA, LPFA, and LTI. There are studies in the literature with and without significant differences in LPTA and LPFA between groups with and without patellar chondromalacia.^{2,4,14} Yeniçeri et al¹⁴ did not find any difference between the groups with and without patellar chondromalacia for LPTA. However, in another study, patellar chondromalacia was found to be associated with increased LPTA.² In the study of Gürsoy et al¹⁴ there was no significant difference for LPFA between the groups with and without patellar chondromalacia. These differences in results between studies may be due to body characteristics such as age, gender, and body mass index of the patient population.

One of the limitations of our study is that the study was retrospective, and the cases were not asymptomatic. The causes of chondromalacia might have been developed for another reason. Although we excluded moderate-severe joint degeneration cases, degenerative cartilage changes might have affected our results. The absence of arthroscopic confirmation or the presence of chondromalacia is another limitation. Since the presence of chondromalacia by the radiologist who had made the anatomical measurements could have been evaluated from the MR images, bias might have been developed.

In conclusion, we demonstrated morphological differences between the groups with and without patellar chondromalacia. The PPTA and age were found to be significantly different between these groups. In addition, the median age was higher in patients with high-grade chondromalacia. It should be kept in mind that demographic differences and anatomical variations may be a cause of patellar chondromalacia.

Ethics Committee Approval: Ethics committee approval was received for this study from the ethics committee of İzmir Democracy University Buca Seyfi Demirsoy Training and Research Hospital (Date: December 28, 2022, Number: 2022/12-124).

Informed Consent: Due to the retrospective design of the study, informed consent was not taken.

Peer-review: Externally peer-reviewed.

Author Contributions: Concept – C.U., A.H.Ç., Ö.T.; Design – C.U., A.H.Ç.; Supervision – B.D.M., Ö.T.; Materials – C.U., A.H.Ç.; Data Collection and/or Processing – C.U.; Analysis and/or Interpretation – A.H.Ç., O.S.; Literature Search – C.U., A.H.Ç., O.S.; Writing Manuscript – C.U., A.H.Ç., O.S., B.D.M., Ö.T.; Critical Review – B.D.M., Ö.T.

Declaration of Interests: The authors declare that they have no competing interest.

Funding: The authors declare that this study had received no financial support.

REFERENCES

1. Jibri Z, Jamieson P, Rakhra KS, Sampaio ML, Dervin G. Patellar maltracking: an update on the diagnosis and treatment strategies. *Insights Imaging*. 2019;10(1):65. [\[CrossRef\]](#)
2. Cilengir AH, Cetinoglu YK, Kazimoglu C, et al. The relationship between patellar tilt and quadriceps patellar tendon angle with anatomical variations and pathologies of the knee joint. *Eur J Radiol*. 2021;139:109719. [\[CrossRef\]](#)
3. Mehl J, Feucht MJ, Bode G, Dovi-Akue D, Südkamp NP, Niemeyer P. Association between patellar cartilage defects and patellofemoral geometry: a matched-pair MRI comparison of patients with and without isolated patellar cartilage defects. *Knee Surg Sports Traumatol Arthrosc*. 2016;24(3):838-846. [\[CrossRef\]](#)
4. Gürsoy M, Dirim Mete B, Oyar O, et al. The association of patellar maltracking with infrapatellar fat pad edema and chondromalacia patella: a quantitative morphological magnetic resonance imaging analysis. *Turk J Phys Med Rehabil*. 2018;64(3):246-252. [\[CrossRef\]](#)
5. Kim JH, Lee SK, Jung JY. Superolateral Hoffa's fat pad oedema: relationship with cartilage T2* value and patellofemoral maltracking. *Eur J Radiol*. 2019;118:122-129. [\[CrossRef\]](#)
6. Ambra LF, Hinckel BB, Arendt EA, Farr J, Gomoll AH. Anatomic risk factors for focal cartilage lesions in the patella and trochlea: a case-control study. *Am J Sports Med*. 2019;47(10):2444-2453. [\[CrossRef\]](#)
7. Higgins LD. Patient evaluation. In: Cole BJ, Malek MM, eds. *Articular Cartilage Lesions: A Practical Guide to Assessment and Treatment*. New York: Springer; 2004:13-21.
8. Grelsamer RP, Weinstein CH, Gould J, Dubey A. Patellar tilt: the physical examination correlates with MR imaging. *Knee*. 2008;15(1):3-8. [\[CrossRef\]](#)
9. Barbier-Brion B, Lerais JM, Aubry S, et al. Magnetic resonance imaging in patellar lateral femoral friction syndrome (PLFFS): prospective case-control study. *Diagn Interv Imaging*. 2012;93(3):e171-e182. [\[CrossRef\]](#)
10. Subhawong TK, Eng J, Carrino JA, Chhabra A. Superolateral Hoffa's fat pad edema: association with patellofemoral maltracking and impingement. *AJR Am J Roentgenol*. 2010;195(6):1367-1373. [\[CrossRef\]](#)
11. Jibri Z, Martin D, Mansour R, Kamath S. The association of infrapatellar fat pad oedema with patellar maltracking: a case-control study. *Skelet Radiol*. 2012;41(8):925-931. [\[CrossRef\]](#)
12. Damgacı L, Özer H, Duran S. Patella-patellar tendon angle and lateral patella-tilt angle decrease patients with chondromalacia patella. *Knee Surg Sports Traumatol Arthrosc*. 2020;28(8):2715-2721. [\[CrossRef\]](#)
13. Kim T, Kim JK, Lee HS, Kim DK. Patella-patellar tendon angle in relation to the medial patellar plica syndrome, chondromalacia patella, and infrapatellar fat pad syndrome. *PLoS One*. 2022;17(3):e0265331. [\[CrossRef\]](#)
14. Yeniçeri Ö, Çullu N, Yeniçeri EN, Kılınc RM, Deveer M, Canbek U. Patellofemoral uyum ve patella tipi ile kondromalazi arasındaki ilişki [Article in Turkish]. *Muğla Sıtkı Koçman Univ Tıp Derg*. 2015;2(2):44-50.

Magnetic Resonance Imaging Assessment of Normal ADC Values of the Parotid Gland

Ömer Kazcı¹, Bünyamin Ece²

¹Department of Radiology, Ankara Training and Research Hospital, Ankara, Turkey

²Department of Radiology, Kastamonu University, Faculty of Medicine, Kastamonu, Turkey

Cite this article as: Kazcı Ö, Ece B. Magnetic resonance imaging assessment of normal ADC values of the parotid gland. *Current Research in MRI*, 2023;2(1):16-18.

These authors contributed equally to this work.

Corresponding author: Ömer Kazcı, e-mail: omerkazci1990@gmail.com

Received: February 16, 2023 **Accepted:** March 15, 2023 **Publication Date:** April 27, 2023

DOI:10.5152/CurrResMRI.2023.23053



Content of this journal is licensed under a Creative Commons Attribution-NonCommercial 4.0 International License.

Abstract

Objective: The objective of this study is to determine the normal Apparent Diffusion Coefficient (ADC) values of the parotid gland in relation to age and gender.

Methods: Fifty female and 50 male patients of the same age were retrospectively analyzed. After inspecting the parotid glands of patients from the same age range, measurements were made using a 30 mm² Region of Interest (ROI) in the superficial region. The research was conducted by a single radiologist.

Results: There is no difference between average ages of men and women ($P = .844$). There was no difference between mean ADC values of men and women ($P = .715$). The average ADC for the entire group was $1069.1 \pm 89.5 \text{ mm}^2/\text{s}$.

Conclusion: In our study, the average ADC for the entire group was $1069.1 \pm 89.5 \text{ mm}^2/\text{s}$. If these values are considered in accordance with the device, technique, age, and gender and used as a reference, hypocellular formations can be anticipated above this value and hypercellular formations below this value.

Keywords: ADC value, parotid, magnetic resonance imaging, normal

INTRODUCTION

The parotid gland is the largest of the 3 pairs of major salivary glands in the human body. It is located in front of and just below the ear, and it produces saliva that is released into the mouth through the parotid duct. The parotid gland plays an important role in the digestive process, as it secretes enzymes that help break down food and also helps to lubricate the mouth and throat to aid in swallowing. However, the parotid gland can also be affected by various diseases, such as infections, tumors, and autoimmune disorders, which can cause swelling, pain, and other symptoms. There are various conditions that can be associated with parotid gland masses. The majority of parotid gland masses are benign tumors such as pleomorphic adenomas, Warthin tumors, or oncocytomas. These tumors are slow-growing, well-defined, and can be easily treated with surgical excision. Malignant tumors of the parotid gland are less common but can be more aggressive. They include mucoepidermoid carcinomas, adenoid cystic carcinomas, and acinic cell carcinomas. These tumors require a combination of surgery, radiation therapy, and sometimes chemotherapy for treatment. Infections of the parotid gland can cause swelling and pain, leading to the development of a mass. The most common cause of parotid gland infection is a viral infection, such as mumps. Bacterial infections can also occur, usually as a complication of a salivary duct stone or other obstruction. Sialolithiasis is a condition where a stone forms in the salivary gland or duct, causing obstruction and leading to swelling and pain. This can also lead to the development of a parotid gland mass. Sjogren's syndrome is an autoimmune disorder that can cause inflammation and destruction of the salivary glands, including the parotid gland. This can lead to the development of a mass and is typically treated with immunosuppressive therapy. Lymphoma is a type of cancer that can affect the lymphatic tissue in the parotid gland, leading to the development of a mass. Treatment typically involves a combination of chemotherapy and radiation therapy. In general, parotid gland masses can be associated with a wide range of conditions, and a thorough evaluation by a qualified healthcare provider is necessary to determine the underlying cause and an appropriate management plan.

A range of radiological imaging techniques can be used to assess the parotid gland. Ultrasonography is performed initially due to its low cost and accessibility. Afterward, if necessary, computed tomography (CT) and magnetic resonance (MR) scans are performed. Magnetic resonance imaging (MRI) lacks ionizing radiation and provides great resolution of soft tissue. It is one of the most prevalent methods. Dynamic series and multiparametric parotid MRI with diffusion can yield data that is nearly as precise as histology.¹ Diffusion Weighted Imaging (DWI)-MRI is a non-invasive imaging technique that measures the diffusion of water molecules in tissue, providing information about tissue cellularity, viscosity, and membrane integrity. ADC is a quantitative parameter derived from DW-MRI that reflects the rate and magnitude of water diffusion in tissue. ADC values have been shown to correlate with various pathological conditions in the parotid gland, such as inflammation, fibrosis, neoplasms, and radiation-induced changes. The classification of parotid tumors is essential. Measurements of ADC (appearance diffusion coefficient) vary in

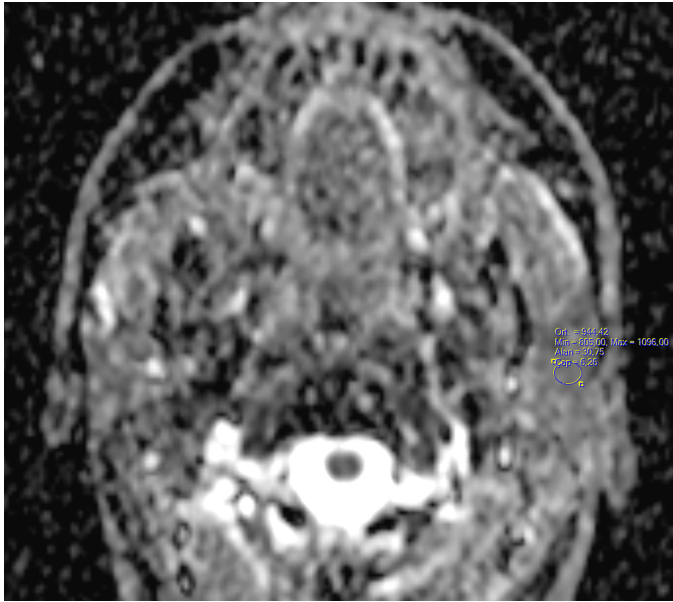


Figure 1. A 17-year-old female patient's left parotid gland superficial segment was assessed for ADC using a 30 mm² ROI.

connection to various diseases and mass types. The objective of this study is to determine the normal ADC values of the parotid gland in relation to age and gender.

METHODS

Since our investigation is retrospective, Bilkent City Hospital Ethics Committee (Date: July 28, 2022, No: E2-22-1105) has been obtained. Since this is a retrospective study, consent was not obtained from patients. Utilizing 1.5 Tesla (Magnetom Aera, Siemens Healthcare, Erlangen, Germany). In our database, neck MRI tests over the previous 5 years were reviewed retrospectively. Fifty patients of the same gender and age were studied. The parotid glands of the selected individuals are homogeneous, and no history of mass infection, radiation to the head and neck, or nontreatment is present. After inspecting the parotid glands of patients from the same age range, measurements were made using a 30 mm² ROI in the superficial region (Figures 1 and 2). The research was conducted by a single radiologist.

As final data, measurements of 50 female and 50 male patients' parotid gland ADC values were recorded and assessed.

RESULTS

In the study, 50 women and 50 men were included. The ages of the female participants ranged from 16 to 87 years. The average age of women was 44.4 ± 17.1 years. Male participation ranged in age between 17 and 88. The average age of males was 45.1 ± 17.5 years.

MAIN POINTS

- The aim of this study is to evaluate the normal ADC value and comparison with different parotid mass lesions.
- The normal ADC values vary by age, gender, and device characteristics.
- The average ADC for the entire group in our investigation was 1069.1 ± 89.5 mm²/s.

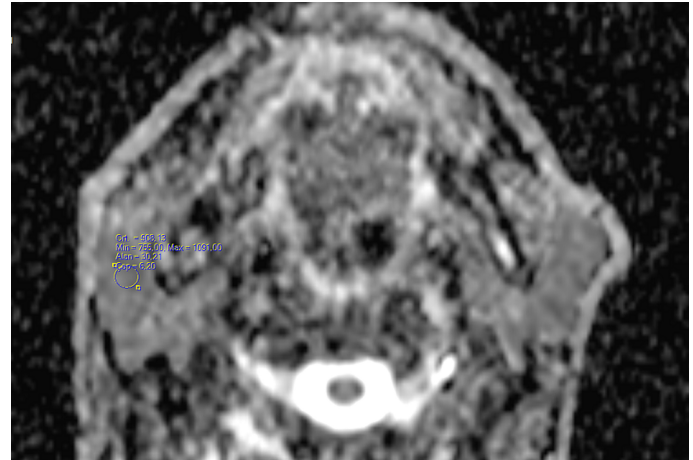


Figure 2. A 58-year-old male patient's right parotid gland superficial segment was assessed for ADC using a 30 mm² ROI.

Table 1. Female and Male Patient Ages and ADC Values

	Total (n=100)	Female (n=50)	Male (n=50)	P
Age				
Mean \pm SS	44.8 ± 17.2	44.4 ± 17.1	45.1 ± 17.5	.844
Min.-Max	16-88	16-87	17-88	
ADC				
Mean \pm SS	1069.1 ± 89.5	1072.4 ± 89.4	1065.8 ± 90.3	.715

There is no difference between men's and women's average ages ($P=.844$). There was no difference between men's and women's mean ADC values ($P=.715$).

The average ADC for the entire group was 1069.1 ± 89.5 mm²/s. The average ADC for the female group was 1072.4 ± 89.4 mm²/s. The average ADC for the male group was 1065.8 ± 90.3 mm²/s ($P=.715$).

Table 1 displays all values stated in the previous paragraph.

DISCUSSION

The largest of the salivary glands is the parotid gland. Due to its superior soft tissue contrast and ability to offer functional information, MRI is a popular method for examining the parotid gland. DWI, which assesses the diffusion of water molecules inside tissues, is one of the functional MRI techniques utilized to evaluate the parotid gland. ADC is generated from DWI and gives an indirect measurement of tissue cellularity and extracellular space.

The normal ADC value of the parotid gland has been reported to be in the range of $1.5\text{--}2.5 \times 10^{-3}$ mm²/s.^{2,3} However, the specific ADC values can vary depending on several factors, such as the imaging protocol, magnetic field strength, and software used for image analysis. For instance, a study by Vandecaveye et al⁴ reported a mean ADC value of 1.85×10^{-3} mm²/s for the parotid gland at 3T, while a study by Lee et al⁵ reported a mean ADC value of 1.5×10^{-3} mm²/s at 1.5 T.

Zhang et al.⁶ report that the typical ADC value for the parotid gland is 0.94 (0.88–0.96) 103 mm²/s, as reported by Ali EL-Adalany et al.⁷ and lower than the ADC values determined with readout-segmented procedures within malignant lesions in previous studies.⁸

The average ADC for the entire group in our investigation was $1069,1 \pm 89.5 \text{ mm}^2/\text{s}$.

If the parotid gland is affected by a disease, like inflammation or a tumor, this could change the ADC readings. Takagi et al⁹ discovered that the ADC values of parotid glands with Sjogren's syndrome, an autoimmune illness that affects the salivary glands, were much lower than the ADC values of parotid glands with normal salivary gland function. In a separate study, Abdel Razek et al² found that the ADC values of normal parotid glands were much higher than those of tumors. Typically, pleomorphic adenomas show elevated ADC values, indicating that the tumor is hypocellular. Unlike carcinomas, which have low ADC values and are hypercellular,¹⁰ this condition is characterized by high ADC values.

Study Limitations

Although ADC values can provide useful information about the tissue characteristics of the parotid gland, their interpretation has several limitations, including technical variability, physiological factors, and pathological conditions. Therefore, the use of standardized imaging protocols, ROI placement, and clinical correlation is necessary for accurate and consistent ADC measurements.

In our study, the average ADC for the entire group was $1069,1 \pm 89.5 \text{ mm}^2$. If these values are considered in accordance with the device, technique, age, and gender and used as a reference, hypocellular formations can be anticipated above this value and hypercellular formations below this value.

Ethics Committee Approval: Ethics committee approval was received for this study from the ethics committee of Bilkent City Hospital (Date: July 28, 2022, Number: E2-22-1105).

Informed Consent: Due to the retrospective design of the study, informed consent was not taken.

Peer-review: Externally peer-reviewed.

Author Contributions: Concept – Ö.K.; Design – Ö.K.; Supervision – Ö.K.; Resources - B.E.; Materials – Ö.K.; Data Collection and/or Processing – Ö.K.; Analysis and/or Interpretation – B.E.; Literature Search – B.E.; Writing – Ö.K.; Critical Review – B.E.

Declaration of Interests: The authors have no conflict of interest to declare.

Funding: The authors declared that this study has received no financial support.

REFERENCES

1. Elmokadem AH, Abdel Khalek AM, Abdel Wahab RM, et al. Diagnostic accuracy of multiparametric magnetic resonance imaging for differentiation between parotid neoplasms. *Can Assoc Radiol J*. 2019;70(3):264-272. [\[CrossRef\]](#)
2. Razek AA, Elkharmy S. Diagnosis of salivary gland tumors. *Expert Rev Anticancer Ther*. 2015;15(5):541-550.
3. Vandecaveye V, De Keyser F, Vander Poorten V, et al. Head and neck squamous cell carcinoma: value of diffusion-weighted MR imaging for nodal staging. *Radiology*. 2009;251(1):134-146. [\[CrossRef\]](#)
4. Lee NK, Kim S, Kim HS, et al. Salivary gland tumors: evaluation with two-phase helical CT. *Radiology*. 2002;224(1):181-186.
5. Razek AA, Sadek AG, Kombar OR, Elmahdy TE, Nada N. Role of apparent diffusion coefficient values in differentiation between malignant and benign solitary thyroid nodules. *AJNR Am J Neuroradiol*. 2008;29(3):563-568. [\[CrossRef\]](#)
6. Zhang Q, Wei Y-M, Qi YG, Li BS. Early changes in apparent diffusion coefficient for salivary glands during radiotherapy for nasopharyngeal carcinoma associated with xerostomia. *Korean J Radiol*. 2018;19(2):328-333. [\[CrossRef\]](#)
7. Ali EL-Adalany M, Mousa AEM, Metwally DEL. The diagnostic value of combined dynamic contrast-enhanced MRI (DCE-MRI) and diffusion-weighted imaging (DWI) in characterization of parotid gland tumors. *Egypt J Radiol Nucl Med*. [\[CrossRef\]](#)
8. Friedli I, Crowe LA, De Perrot TB, et al. Comparison of readout-segmented and conventional single-shot for echo-planar diffusion-weighted imaging in the assessment of kidney interstitial fibrosis. *J Magn Reson Imaging*. 2017;46(6):1631-1640. [\[CrossRef\]](#)
9. Takagi S, Kudo Y, Abe Y, et al. Apparent diffusion coefficient in normal parotid gland and in Sjögren syndrome: association with related autoantibodies. *Radiology*. 2015;277(3):799-806. [\[CrossRef\]](#)
10. Kato H, Kanematsu M, Mizuta K, Ito Y, Hirose Y. Carcinoma ex pleomorphic adenoma of the parotid gland: radiologic-pathologic correlation with MR imaging including diffusion-weighted imaging. *AJNR Am J Neuroradiol*. 2008;29(5):865-867. [\[CrossRef\]](#)

Case Report and Review of Literature of Van-Neck Odelberg Disease: A Challenging Differential Diagnosis for Pelvic Fractures

Nur Hürsoy^{ID}, Lütfullah Sağır^{ID}, Elif Arzu Özen^{ID}, Fatma Beyazal Çeliker^{ID}

Department of Radiology, Recep Tayyip Erdoğan University, Faculty of Medicine, Rize, Turkey

Cite this article as: Hürsoy N, Sağır L, Özen EA, Beyazal Çeliker F. Case report and review of literature of van-neck odelberg disease: A challenging differential diagnosis for pelvic fractures. *Current Research in MRI*, 2023;2(1):19-21.

Corresponding author: Nur Hürsoy, e-mail: nur.hursoy@erdogan.edu.tr

Received: January 9, 2023 **Accepted:** March 24, 2023 **Publication Date:** April 29, 2023

DOI:10.5152/CurrResMRI.2023.23037



Content of this journal is licensed under a Creative Commons Attribution-NonCommercial 4.0 International License.

Abstract

Ischiopubic synchondrosis is a temporary joint, and this joint's swelling can be presented with pelvic pain in adolescents. Even though there is some hypothesis about this condition, histopathology is unclear. Because of the broad differential diagnosis list of pelvic pain, the awareness of this entity is essential to provide the unnecessary procedures. We have presented 2 cases of that condition with imaging findings.

Keywords: Ischiopubic synchondrosis, osteochondritis, Van Neck–Odelberg disease

INTRODUCTION

Pelvic pain is a common and essential problem in children, especially after trauma. Magnetic resonance imaging (MRI) is a preferred imaging modality because of the lack of radiation, but the findings often can be unspecific. For example, fractures, benign and malignant tumors, and osteomyelitis may be seen as bone marrow edema. Most differential diagnoses require additional processes such as computed tomography or biopsy.

Synchondroses are temporary joints that obliterate before puberty by the bony union of synostosis. Ischiopubic synchondrosis (IPS) can be seen before the fusion of ischial and pubic bones as a radiolucent swelling on radiographs and is considered a normal variant. IPS is typically characterized by the detection of bone marrow edema and ting soft tissue edema on MRI. Consequently, unilateral findings of such nature may be misconstrued as pathological disorders

Sometimes, synchondrosis closure may be painful, and this entity was described with imaging findings by Odelberg and van Neck in the 1920s.² We have presented 2 cases of van Neck–Odelberg disease.

CASE PRESENTATIONS

Case 1

An 8-year-old girl was evaluated because of right hip pain for 3 days. There was no trauma history, and laboratory findings were normal. The MRI was obtained for suspected Perthes disease. Expansion of IPS with perilesional edema was seen on MR sequences (Figure 1). There was no abnormality on the femoral head, and the hip joint was also normal.

Case 2

A 4-year-old boy was diagnosed with osteomyelitis in the right limb (Figure 2). He had an abscess and edema surrounding his tibia at present. Because he complained of left groin pain after 8 months of treatment, a left hip MRI was acquired. There was asymmetrical soft tissue edema surrounding IPS (Figure 3).

DISCUSSION

Differential diagnosis of bone marrow edema includes osteomyelitis, stress reactions—fractures, and malignant infiltrations. Especially if the pain is present, clinical and radiological findings could be a significant challenge. However, evaluating these findings with the right aspects made management more effortless.

Ischiopubic synchondrosis is a temporary joint that can be seen before skeletal maturation. There are 2 ossification centers and a cartilaginous center, and at the pre-pubertal period, bilateral enlargement of the synchondrosis is normal.³

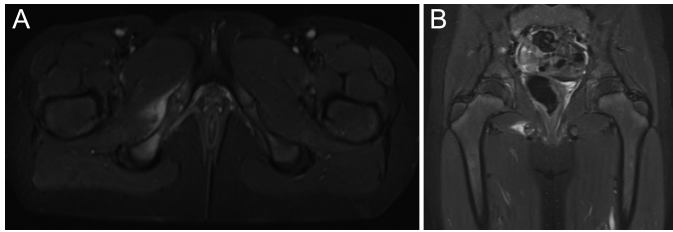


Figure 1. (A, B) Axial and coronal T2-weighted magnetic resonance images. Signal intensities are compatible with soft tissue edema at the surrounding muscles of the right ischiopubic synchondrosis. Enlargement and minimal irregularity of right ischiopubic synchondrosis are detected when comparing left side.

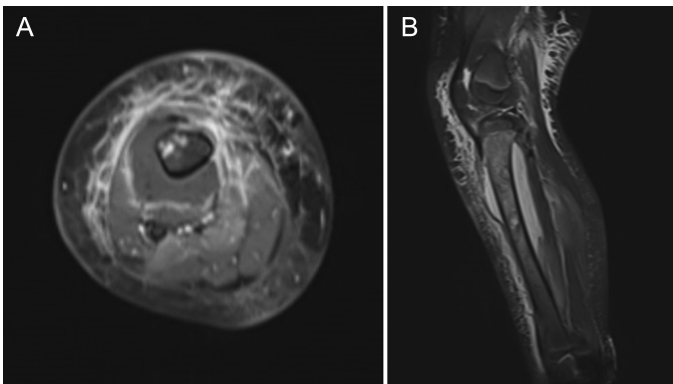


Figure 2. (A, B) Gadolinium contrast-enhanced fat-suppressed axial T1-weighted and coronal T2a-weighted crural magnetic resonance images. Subperiosteal abscess with peripheral contrast enhancement and bone marrow edema at the proximal half of the tibia indicate osteomyelitis.

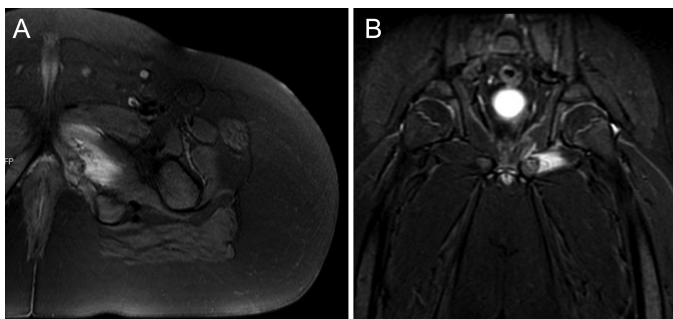


Figure 3. (A, B) Axial and coronal T2-weighted magnetic resonance images of the contralateral side of osteomyelitis. Soft tissue edema at the adjacent muscles to left ischiopubic synchondrosis. Imaging findings are similar to Figure 1A, B.

Swelling at the ischiopubic fusion zone on plain radiographs was accepted as a normal variant before puberty. Nevertheless, an asymmetrical appearance could be seen, probably because of unbalanced

mechanical stress—the pain at this joint with or without limitation in a movement named van Neck–Odelberg disease. Although even the main etiopathogenesis of this disease is not certain, it is characterized by osteochondritis of the ischiopubic ramus, and with symptomatic treatment, patients recover in a few weeks.^{4,5} There are different views about the relationship between IPS and the dominant leg in literature. In some case reports, patients complain about the contralateral side of imaging findings.^{6–8} In particular, for case 2, the leading cause may be the weight load on the left side due to the inability to use the right limb.

The literature reports cases of IPS in patients ranging from 3.5 to 15 years of age.^{2,4–7,9–16} The youngest recorded patient was a 3.5-year-old girl with a dislocated right hip and IPS on the left side.¹ Most cases reported in the literature were between 6 and 8 years old. In the study of Herneth et al.⁸ the estimated median age was 7.5 years. Out of the 15 reported cases, 11 were male, but there was no male predominance in one study about IPS.¹⁷

The primary complaint of patients with IPS is pain in the gluteal or groin area on the affected side. There are no specific examination findings, but it is interesting to note that 3 patients were found to be obese.^{3,6,11} Being overweight may be considered a risk factor for IPS.

The critical point is the exclusion of other clinical entities which may cause pelvic pain, like inflammatory arthritis, pathological fractures, osteomyelitis, and sarcoma.¹⁰ Every possibility should be kept in mind for early diagnosis, but, on the other hand, overdiagnosis should be avoided. Investigation revealed that elevated inflammatory markers and positive blood cultures could help the diagnosis of osteomyelitis and juvenile inflammatory arthritis. Excessive exercise habits should be interrogated in the patient's history, and serum calcium and vitamin D levels should be examined to determine the risk of pathologic fractures. The absence of lytic lesions on radiographs helps exclude Ewing sarcoma, but if there is a doubt about the diagnosis, follow-up imaging must recommend.

The MRI helps rule out other differential diagnoses and reduces ionizing radiation imaging in patients with van Neck–Odelberg disease.^{17,18} The awareness of physiologic or benign conditions of the musculoskeletal system in childhood is essential to avoid unnecessary interventions and additional imaging.

Informed Consent: Written informed consent was obtained from patients who participated in this study.

Peer-review: Externally peer-reviewed.

Author Contributions: Concept – N.H.; Design – N.H., E.A.Ö.; Supervision – F.B.Ç.; Resources – N.H., E.A.Ö., L.S.; Materials – E.A.Ö., L.S.; Data Collection and/or Processing – E.A., L.S.; Analysis and/or Interpretation – N.H., F.B.Ç.; Literature Search – N.H.; Writing Manuscript – N.H., F.B.Ç., E.A.Ö., L.S.; Critical Review – F.B.Ç.

Declaration of Interests: The authors declare that they have no competing interest.

Funding: There is no financial support.

REFERENCES

- Herneth AM, Trattinig S, Bader TR, et al. MR imaging of the ischiopubic synchondrosis. *Magn Reson Imaging*. 2000;18(5):519-524. [\[CrossRef\]](#)
- MacArini L, Lallo T, Milillo P, Muscarella S, Vinci R, Stoppino LP. Case report: multimodality imaging of van Neck–Odelberg disease. *Indian J Radiol Imaging*. 2011;21(2):107-110. [\[CrossRef\]](#)

MAIN POINTS

- Van Neck–Odelberg disease may be present with hip pain in children.
- Magnetic resonance imaging and laboratory findings can help exclude other possibilities.
- Overuse of one side of the legs may cause this entity.

3. Aubry S, Chateil JF. Pediatric radiology. *J Radiol.* 2006;87(7-8):899-905. [\[CrossRef\]](#)
4. Ceri L, Sperati G. Van Neck-Odelberg disease in a 8-year-old children: a rare case report. *Acta Biomed.* 2020;91(4-S):238-240. [\[CrossRef\]](#)
5. Morante Bolado I, Ortega Navaridas M, Clemente Garulo D, López Robledillo JC. Van Neck-Odelberg disease: another cause of limp in childhood. *Reumatol Clin.* 2017;13(5):299-300. [\[CrossRef\]](#)
6. Beyitler İ, Kavukcu S. A case of van Neck-Odelberg disease and intermittent overuse injury. *Arch Rheumatol.* 2016;31(4):381-383. [\[CrossRef\]](#)
7. Camacho DAH, Bernal P, Cifuentes L, Rivero O. Van Neck–Odelberg disease: a rare cause of pain in pediatric pelvis. *World J Nucl Med.* 2020;19(4):435-437. [\[CrossRef\]](#)
8. Herneth AM, Philipp MO, Pretterklieber ML, Balassy C, Winkelbauer FW, Beaulieu CF. Asymmetric closure of ischiopubic synchondrosis in pediatric patients: correlation with foot dominance. *AJR Am J Roentgenol.* 2004;182(2):361-365. [\[CrossRef\]](#)
9. Narayanan SA, Chandy LJ, Kandathil JC. Van Neck disease: a rare case. *Case Rep Orthop Res.* 2021 January 25 Cited 2023 Mar 4;4(1):39-42. [\[CrossRef\]](#)
10. Sabir N, Çakmak P, Yılmaz N, Yüksel S. Osteochondrosis of ischiopubic synchondrosis: van Neck–Odelberg disease. *J Pediatr.* 2021;229(February):307-308. [\[CrossRef\]](#)
11. Oliveira F. Differential diagnosis in painful ischiopubic synchondrosis (IPS): a case report. *Iowa Orthop J.* 2010;30:195-200.
12. Sandomenico C, Tamburrini O. Bilateral accessory ossification center of the ischio-pubic synchondrosis in a female infant. Follow-up for over a three year period. *Pediatr Radiol.* 1981;10(4):233-236. [\[CrossRef\]](#)
13. Chaudhari AP, Shah G, Patil SS, Ghodke AB, Kelkar SB. Van Neck-Odelberg disease: a rare case report. *J Orthop Case Rep.* 2017 January-February;7(1):24-27. [\[CrossRef\]](#)
14. Fonseca JP, Figueiredo P, Pinheiro JP. Osteochondroses in children's sports practice – a rare case of van Neck–Odelberg disease. *JRM-CC.* 2022;5:jrmcc00090. [\[CrossRef\]](#)
15. Korkmazer S, Kaptan AY, Eren TK, Sepetçi Ö, Tekpınar İ, Tıraş HM. A rare disease of the pediatric pelvis: van Neck-Odelberg disease. *Jt Dis Relat. Surg Case Rep.* 2022;1(1):15-18.
16. Jose J, Smith MK, Silverman E, Lesniak BP, Kaplan LD. Stress injuries of the ischiopubic synchondrosis. *Am J Orthop (Belle Mead NJ).* 2013;42(3):127-129.
17. Schneider KN, Lampe LP, Gosheger G, et al. Invasive diagnostic and therapeutic measures are unnecessary in patients with symptomatic van Neck–Odelberg disease (ischiopubic synchondrosis): a retrospective single-center study of 21 patients with median follow-up of 5 years. *Acta Orthop.* 2021;92(3):347-351. [\[CrossRef\]](#)
18. Costa E Silva A, Teixeira B, Pereira AC, Almeida E. Van Neck-Odelberg disease: A rare case report. *Port J Pediatr.* 2021;52(4):341-342.